High-resolution modeling of nearshore circulation in an upwelling ecosystem: resolving sub-mesoscale variability

Juan Faúndez, Céline Acary-Robert, Christopher Aiken, Sergio Navarrete, Antoine Rousseau

High-resolution modeling of nearshore circulation in an upwelling ecosystem: resolving sub-mesoscale variability

Juan Faúndez[a,b,*], Céline Acary-Robert[c], Christopher Aiken[e], Sergio Navarrete[a,d,g], Antoine Rousseau[f]

[a] *Estación Costera de Investigaciones Marinas, Pontificia Universidad Católica de Chile, Chile*
[b] *Programa de Doctorado en Ciencias Biológicas, Pontificia Universidad Católica de Chile, Chile*
[c] *Université de Grenoble Alpes, Laboratoire LJK, UMR 5224, France*
[d] *Millennium Nucleus for Ecology and Conservation of Temperate Mesophotic Reef Ecosystems (NUTME), Departamento de Ecología, Pontificia Universidad Católica de Chile, Chile*
[e] *Coastal Marine Ecosystems Research Centre, Central Queensland University, Australia*
[f] *Inria Lemon and IMAG, Univ. Montpellier, CNRS, 34000 Montpellier, France.*
[g] *Marine Energy Research Innovation Center (MERIC), Avda. Apoquindo 2827, Santiago, Chile*

Abstract

While numerical modeling has proven successful at reproducing the physical, chemical, and biological processes associated with circulation over regional and mesoscales, challenges remain for modeling the coastal zone at sufficiently high resolution to resolve coastal flows and their interactions with larger-scale processes. Computational costs associated with grid resolution and limited observations for model validation are important concerns. This study evaluates a climatological hydrodynamic model off central Chile (28-38° S), which has three nested domains to reproduce both the regional and nearshore circulation patterns. To determine whether submesoscale processes propagate up to larger scales, results from the nested High-Resolution Model (HRM2, 32-34°S and 0.87 km resolution) and its parent (HRM0, 28-36°S and 7.4 km) were compared with those from a Low-resolution Model (LRM0) configured with the exact resolution as the HRM0. While both HRM0 and LRM0 reproduced well the climatological Sea Surface Temperature (SST) and Salinity (SSS), as well as the general spatial patterns of kinetic energy, the annual transport of the Peru-Chile Undercurrent (PCUC) increased in the nested HRM0 (-0.7 to -1.3 Sv) compared to the LRMO (-0.58 to -0.95 Sv). Moreover, the Coastal Chilean Current (CCC) became up 2.16 faster in HRM2 than in LRM0, with a sharp shoreward decline in the maximum speed (down to

11 cm/s) nearshore, defining in this manner a coastal boundary layer (CBL), which was not reproduced by the LRM0. Also, the upwelling process in the HRMO was intensified by topographic features and was spatially consistent with ageostrophic circulation patterns. As expected, the most remarkable differences between model resolutions emerged nearshore, especially within the CBL, highlighting the importance of topographic effects on coastal circulation. Thus, although the low-resolution model can reproduce patterns of circulation in the coastal ocean fairly well, resolving submesoscale variability as in the HRMO imposes moderate to large changes in transport, current velocities, vorticity and topographic realism of the upwelling process. The extent to which variation in these processes affects biochemical processes, particle transports, and or larval dispersal must still be investigated.

Keywords: High-resolution modeling, nesting, coastal boundary layer

Introduction

Characterizing circulation patterns over the continental inner-shelf represents an enormous challenge because of the complexity in the underlying physical processes that occur over multiple spatial and temporal scales, largely determined by the interaction between winds, fluids and the rigid coastal topography (Largier, 2003, Kirincich & Barth, 2009, Lentz & Fewings, 2012, Brink, 2016). The challenge to provide useful representations of the coastal circulation becomes even more difficult due to the low frequency of observations that can be gathered over spatial domains and periods of time large and long enough to encompass most of the processes in which we are interested, and for which we would like to build observational and forecasting models. Coastal circulation processes modulate the biological productivity that allows the existence of most pelagic and benthic communities and ecosystems (Connolly et al., 2010, Pitcher et al., 2014, Largier, 2020), the connectivity of populations via dispersal of propagules, which determines persistence of populations and defines local biodiversity (Cowen & Sponaugle, 2009, White et al., 2019), and, in general,

*Corresponding author
Email address: juan.faundez@gmail.com (Juan Faúndez)

the carrying capacity and buffering of all human activities on the coastal ocean. Because of these inherently limited observational capabilities of the coastal marine environment, hydrodynamic three-dimensional modeling continues to be instrumental in making advances in our understanding of coastal circulation in different regions of the world, providing a tool to characterize this complex environment that otherwise would be impossible to explore through observational models alone (Penven et al., 2001, Mitarai et al., 2008, McWilliams, 2016). Multiple modeling approaches, suitable for the coastal ocean, have been developed. They differ in their numerical methods, horizontal and vertical mesh discretization, the manner in which they resolve topography, and the boundary conditions that can be implemented. Additionally, computational advances have made possible the increase in spatial resolution of these models, some of which are able to reproduce important circulation aspects governed by both geostrophic and ageostrophic processes (McWilliams, 2003 , Capet et al., 2008, Soufflet et al., 2016). As with all models, a trade-off exists between model scope or generality, resolution, and realism (eg Levins 1968). The comparatively recent development of computationally-efficient nested numerical models that can resolve complex coastal circulation at multiple scales, attempts to strike a practical balance in this three-prong trade-off, by combining high resolution of processes within section of a more general model. Here we develop a nested model for coastal circulation of a section of the Humboldt Upwelling Ecosystem (HUE), assess its consistency with observations, and demonstrate that the increase in resolution markedly improves the representation of the near-shore circulation with respect to a coarser scale model.

Mesoscale oceanographic processes have remained the focus of hydrodynamic studies in coastal regions of the world, due to both the importance of these processes in hydrographic variability in coastal ecosystems, and to the practical constraints upon the resolution needed to simulate the submesoscale. In the HUE, such models have provided a deeper understanding of the upwelling circulation, topographic intensification, variability of Ekman transport, mesoscale eddy activity, and the effects of riverine inputs, among others (Leth et al., 2004, Dewitte et al., 2008, Aiken et al., 2008 Aguirre et al., 2012, Vergara et al., 2016). The level of realism achieved in these mesoscale models has been sufficient to explore, for in-

stance, the broad consequences for propagule dispersal (Aiken et al., 2007, Parada et al., 2012, Medel et al., 2018, Ospina-Alvarez et al., 2018) or to project effects of climate change (Aiken et al., 2011, Oerder et al., 2015, Lima et al 2021). But the resolution used in these models - with scales on the order of multiple kilometers - limits their applicability to resolve near-shore processes, where strong gradients commonly occur over these same scales within the Coastal Boundary Layer (CBL). A significant body of observational evidence challenges the assumption that the unresolved processes have a negligible impact on the mesoscale (e.g. Nickols et al., 2012 and 2013). The processes that define the dynamics and spatio-temporal scales of variability in coastal environments commonly occur over scales of kilometers and less - often called the submesoscale (Nickols et al., 2013, McWilliams, 2016). As such, these processes can emerge and be correctly represented only by sufficiently increasing model resolution (Liu & Levine, 2016, Sun et al., 2020). Certainly, the presence of these submesoscale structures and the increase in vertical speed associated with different energy transfer mechanisms (Capet et al., 2008a, Mahadevan, 2016) have exclusively been captured by increasing the resolution into observations and models. These structures might affect the cross- and alongshore transport, as well as, the final fate of particles and pollutants in the coastal zone (Harrison et al., 2013, Dauhajre et al., 2017). Indeed, the presence of a nearshore CBL, where an exponential decay of currents speed and a raised eddy diffusivity occurs, can greatly influence the retention and dispersion capacities of nearshore matter (Nickols et al., 2012, Nickols et al., 2015, Morgan, 2014). But beyond these local observations that point to increased importance of submesoscale processes, it is still unclear to what extent they influence the mesoscale circulation. A case in point that has received much attention is the determinant of dispersal and transport between coastal sub-populations of the propagules produced on the shore by adults of largely sedentary species. It has been argued that coastal, small-scale processes may have primacy in determining patterns of dispersal, connectivity and eventual onshore recruitment (Morgan et al., 2009, Nickols et al., 2015, Harrison et al., 2013), over the mesoscale variations typically represented in larval transport simulations, which could potentially misrepresent these important aspects of population and community persistence and productivity (Dauhajre et al., Bani et al., 2021). Therefore,

to realistically simulate dispersal and population connectivity, processes we may require a significant increase in spatial resolution, so that finer coastal topographic complexity and circulation pattern are better captured in the models, but at the same time being able to resolve a domain large enough to capture mesoscale variability. In other words, to assess the importance of resolving the sub mesoscale, numerical models representing the inner shelf circulation should reproduce the mesoscale circulation while still capturing the CBL, whose potential interaction has not commonly been considered in shelf circulation studies along HUE or other upwelling ecosystems.

The eastern margin of the South Pacific Ocean is characterized by a narrow continental shelf where the circulation is mainly forced through seasonal wind variability, modified by topography and the coastline morphology (Thiel et al., 2007, Aiken et al., 2008 Strub et al., 2013). Prevailing equatorward winds drive offshore Ekman transport and the coastal upwelling of subsurface waters, that in turn feeds the formation of energetic mesoscale eddies, meanders and coastal jets (Mesias et al., 2003, Rutllant et al., 2004, Hormazabal et al., 2004, Capet et al., 2004, Chaigneau & Pizarro, 2005). As these processes largely control the rates of continental shelf fertilization and organic matter exportation, understanding their dynamics allows us to explore effects on ecological systems (Letelier et al., 2009, Correa-Ramirez et al., 2007, Gruber et al., 2011, Correa-Ramirez et al., 2012). Here we investigate the importance of high spatio-temporal resolution for correctly reproducing features at submesoscale, such as the CBL, and whether this influences the mesoscale circulation as simulated in lower resolution models, through analysis of a nested model with variable spatial resolution along the coast off central Chile. Our study area is centered within one of the ocean regions with highest biological productivity in the world, supporting a rich and diverse artisanal fishing activity employing several thousand people (Thiel et al., 2007, Castilla, 2010,). The outer and middle shelf circulation has been relatively well characterized through observations (Strub et al., 1995, Shaffer et al., 2004, Hormazabal et al., 2004) and simulations (Leth & Shaffer, 2001, Aguirre et al., 2014). Alongshore, the coastal circulation is strongly controlled by the seasonal equatorward wind stress, which modulates the variability of the coastal upwelling (Sobarzo et al., 2007, Aguirre et al., 2012, Bravo et al., 2016, Astudillo

et al., 2019), the equatorward Chilean Coastal Current (CCC) and the poleward Peru-Chile Undercurrent (PCUC) (Strub et al., 1995, Vergara et al., 2016, Pizarro-Koch et al., 2019). The CCC interaction with the coastline geometry and the bottom topography have been an issue to understand some mechanisms that affect the upwelling intensification and eddy generation (Leth & Middleton, 2004, Aiken et al., 2008). As is the case generally for upwelling ecosystems, the response of the HCU to long-term climate change remains uncertain (Sydeman et al. 2014, Schneider et al., 2017, Aguirre et al, 2018, 2021 Weidberg et al., 2020, Gibson et al., 2007, Chavez & Messié, 2009), which makes it particularly important and urgent to improve our understanding of inner shelf dynamics.

Methods

0.1. Hydrodynamic model

The nearshore circulation over the inner-shelf of central Chile, resolving both coarse and high resolution scales, was simulated using the UCLA Regional Ocean Modelling Systems (ROMS, Shchepetkin & McWilliams, 2005) coupled to the AGRIF package for nesting grids (Adaptive Grid Refinement in Fortran, Debreu et al., 2012) currently known as https://www.croco-ocean.org/ CROCO (Coastal and Regional Ocean Community model).

The model solves the primitive equations under the Boussinesq and hydrostatic approximations, using an explicit 3D ocean free surface scheme, sigma-type vertical coordinates, and a horizontal orthogonal curvilinear system. Two simulations were run over the same domain, covering the region 28°-38°S and 70°-82°W, but with different configurations. The first simulation used a single grid with 1/12° horizontal resolution (7.74 km) and 40 vertical levels in σ-coordinates, and is referred to as the Low-Resolution Model (LRM0). The second simulation used the same coarse grid and vertical levels in σ-coordinates, and was used as the parent (HRM0) of two nested regions. The nested grids were configured with 40 σ-coordinates levels and horizontal resolutions of 2.6 km (HRM1) and 0.87 km (HRM2), whose extensions are shown in the Table1 and Figure 4b. The solutions for each of these nested grids are referred to, respectively, as the parent High-Resolution Model (HRM0), the intermediate High-Resolution Model (HRM1), and the child High-Resolution Model (HRM2).

Communication between the domains in the nested configuration was established through the 2-way nesting method implemented in the AGRIF package (Adaptive Grid Refinement in Fortran, Debreu et al., 2012). This methodology allows solving the interaction between mesoscale and submesoscale processes through a viscosity and diffusion increment as the grid resolution increases.

0.1.1. Nesting Configuration

The Global Relief Model (doi: 10.7289 / V5C8276METOPO1) with a resolution of 1 arc-minute (∼1.85 km) provided the topography for LRM0 and HRM0, while the General Bathymetric Chart of the Oceans (https://www.gebco.net/data$_a nd_p roducts/gridded_b athymetry_d ata/gebco_3 0_s ec$ *secondresolution*(∼0.92 km), was used for the two nested HRM. The bathymetry was interpolated between each nested grid through a bilinear method, and a smoothing algorithm applied on the logarithm of bathymetry to limit pressure gradient errors (Penven et al., 2005). The coordinates between grids were interpolated through a fourth-order polynomial, while the bathymetric connections were carried-out along a three cells border at the same level and then connected by linear interpolation. The fine grids were extrapolated on the HRM0 mask to increase the coastal resolution utilizing a Taylor expansion to minimize the error.

Table 1: Nested domains into the hydrodynamic model. The table describes the name model abbreviation, the domains coordinates, resolutions and the runtime for each simulation.

Model Name Abbreviation	Domain	Resolution (km)	Runtime (yr)
LRM0	28-38°S - 70-82°W	7.74	1 to 20
HRM0	28-38°S - 70-82°W	7.74	1 to 20
HRM1	28.4-35°S - 71.7-75°W	2.63	10 to 20
HRM2	32.4-34.4°S - 71.2-72.2°W	0.87	13 to 20

0.1.2. Initial Conditions and Forcings

The general nearshore circulation and its seasonal variability were reproduced by forcing the model with hydrographic and wind conditions derived from multi-annual climatologies. The LRM0 and HRM0 were forced with a monthly wind stress climatology from http://agate.coas.oregonstate.edu/scow/SCOW (Scatterometer Climatology of Ocean Winds, Risien & Chelton 2008) obtained between 2000-2008 at a resolution of 50 km. The monthly boundary conditions used a temperature and salinity climatology obtained between 1958-2008 from http://apdrc.soest.hawaii.edu/datadoc/soda$_2$.1.6.*phpSODAv*2.1.6(*SimpleOceanDataAs*
AtmosphereDataset.

The LRM0 and the nested HRM0 simulations were run for 20 years. The HRM1 boundary conditions were obtained from the tenth year of the HRM0 and then simulated coupled to HRM0 until the 20th year. Finally, the HRM2 started with the hydrological conditions from the 13th year of the nested HRM0+HRM1 (Table 1). All simulations ran in parallel using 120 processors from the high-speed computing cluster "Leftraru" from the Chilean National Laboratory for High-Performance Computing (NLHPC).

0.1.3. Validation

For validating the ability of the model to reproduce the magnitude of the main oceanographic variables, an annual climatology was calculated between the fourth and tenth years of LRM0. The seasonal averages corresponded to austral summer (December, January, February), autumn (March, April, May), winter (June, July, August), and spring (September, October, November). Model realism was evaluated through comparison of climatological values to satellite products, oceanographic measurements, and reanalysis (AVISO, CARS, and HYCOM, respectively). The climatological eddy kinetic energy (EKE) and its spatial structure were obtained from satellite altimetry data from AVISO (2000-2014) and compared with the LRM0 and HRM0. The EKE was calculated from the surface geostrophic anomaly and the sea surface height following the method of Hormazábal and collaborators (2004), where the geostrophic velocities were computed as:

$$U_g = \frac{-g}{f}\frac{\delta\eta}{\delta y} \quad (1)$$

182

$$V_g = \frac{g}{f}\frac{\delta\eta}{\delta x} \quad (2)$$

183 where U_g and V_g are the anomaly of zonal and meridional geostrophic velocity, respec-
184 tively, g is the gravity, f is the Coriolis parameter, and η is the sea surface height anomaly.
185 Thus, the average of the EKE during the period analyzed is:

$$EKE = \frac{1}{2}[\langle (U_g - \langle U_g \rangle)^2 \rangle + \langle (V_g - \langle V_g \rangle)^2 \rangle] \quad (3)$$

186 where $\langle\rangle$ is the time averaged within each database. Additionally, we calculated the
187 spatial correlation between the LRM0 sea level anomalies and the observations.

The seasonal averages of temperature and salinity from LRM0 were compared with the climatological observations of the CSIRO Atlas of Regional Seas (www.cmar.csiro.au/cars CARS2009, (www.cmar.csiro.au/cars); (Ridgway et al, 2002). Meanwhile, the transport (Sv) for the main alongshore currents, as the CCC and PCUC, were compared between the LRM0, HRM0 and the HYbrid Coordinate Ocean Model reanalysis (http://tds.hycom.org/thredds/dodsC /expt$_9$1.1$-lex.europa.eu[HYCOM; (Chassignetetal.2007)betweentheyears2000to2010fromtheexperim$

188 *Resolution dependence of the nearshore circulation*

189 The effect of the increasing the resolution of the nearshore was assessed by calculating
190 geostrophic and ageostrophic EKE on the HRM2, and comparing it against the LRM0. The
191 ageostrophic EKE was estimated by the difference between the geostrophic EKE and the
192 EKE determined directly by both components of the simulated currents velocities. Addi-
193 tionally, the difference between sea surface temperature and the components of the currents
194 velocity were determined by downscaling the HRM2 to the LRM0 resolution.

195 Differences due to model resolution in the vertical profile and transport of the PCUC
196 and CCC were determined by analyzing crosshore transects at sites identified in previ-
197 ous observational studies as areas of intensification or weakening of upwelling (e.g. Tapia
198 et al., 2009), Papudo (PA), Punta Curaumilla (PC), Las Cruces (LC), Punta Toro (PT)

and Topocalma (TO). The seasonal variability of the CCC, and the existence of a CBL, was evaluated through analysis of the alongshore current transects across the continental shelf (from the coast to the 200 m isobath) at 51 locations between 32.4°S and 34.4°S. The former was identified by the maximum in along-shore velocity, and the latter by the location of the most rapid decrease in along-shore velocity below the average seasonal speed. The nearshore circulation inside the CBL for the HRM2 and LRM0 were analyzed during a short favorable upwelling period (16-27 December, nineteenth year), through the current frequency distribution normalized by the total number of observations and the bin width. Then, the frequency distribution described the relative vorticity normalized by the Coriolis parameter (ζ/f) and the vertical and horizontal velocities in 2, 10, 20, 30, 40 and 60 m. An investigation of the mechanisms involved in the upwelling or downwelling processes over the inner-shelf in front of the same sites described above was used to determine the causes for the resolution-related differences observed in the near-shore circulation.

Results

The large-scale circulation was examined through three cross-shore transects showing the alongshore flows obtained from the LRM0 (Fig. 1a-c) and HRM0 (Fig. 1d-f) at 30°, 33° and 36°S from the coastline to 450 km offshore. Both coarser grids reproduced a dominant surface nearshore flow which is consistent with the Chilean Coastal Current (CCC) (Shaffer et al., 1995). This current was characterized by an equatorward flow that reached in the LRM0 a maximum annual speed of 8.1±2.1 cm/s across 36°S, and an lower layer depth ranged at 94 to 164 meters, becoming progressively shallower and narrow (64 to 46 km) downstream (Table 2). On the other hand, the nested HRM0 presented a slower maximum current speed across 33°S (6.7±1.6 cm/s) and similarly to the LRM0, the CCC became shallower and narrow downstream, where the lower layer ranged in 73 to 173 meters and layer width varying between 41 to 63 km (Table 2). The CCC transport decreased equatorward without important difference in the annual average between the coarser grids (0.48 to 0.19 Sv and 0.4 to 0.17 Sv for the LRM0 and HRM0, respectively). Most transport seemed to be concentrated during winter-spring period, where the average transport reached 0.68 Sv

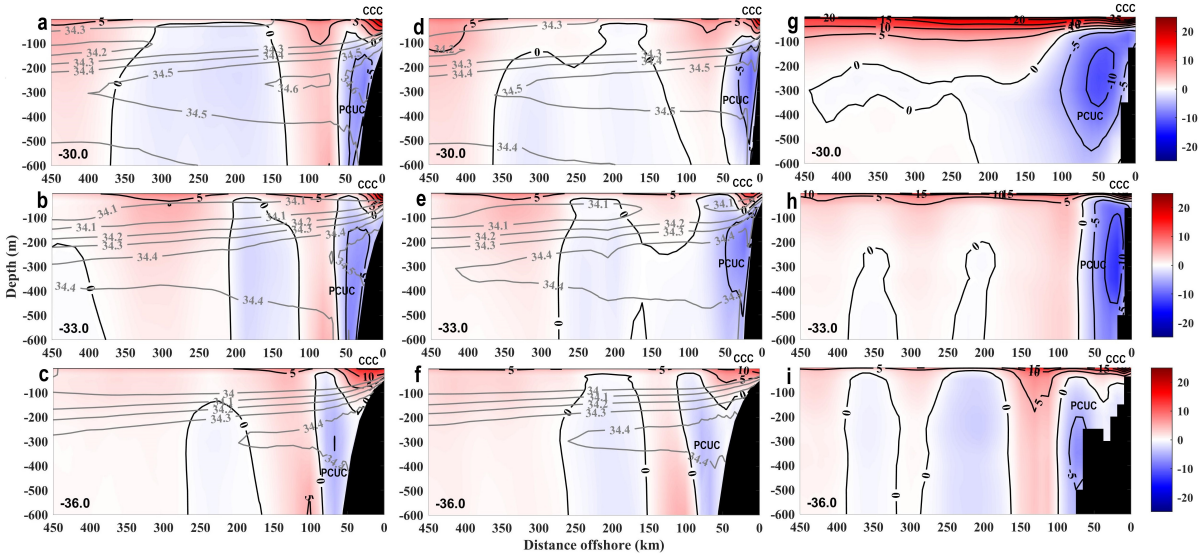

Figure 1: Offshore transects across 30°, 33° y 36°S contrasting the simulated alongshore current (cm/s) from LRM0 (a, b y c), HRM0 (d, e y f) and HYCOM (g, h y i), respectively. The model reproduce the main currents in the Humboldt system, such as the CCC and the PCUC. The contours describe the current speed (black line) and the salinity (gray line)

in the LRM0 and 0.66 Sv in the HRM0 around 36°S. Meanwhile, the maximum transport in 30°S took place in spring with 0.25 Sv in the LRM0 and 0.34 Sv in the HRM0 (Table 2). Comparing our simulations with the transport estimated for HYCOM (Fig. 1g-i), the reanalysis resulted quite similar at 36°S (ca 8% weaker), but transported 0.9 and -0.3 fold the observed in HRM0 at 30 and 33°S, respectively (See Table 2). When the resolution increased through the HRM2, the CCC showed a cross-shore narrowing and deepening equatorwards, accelerating currents upstream of 33.5°S (i.e., Topocalma site) (Fig. 2). These trends were stronger in the HRM2 than the LRM0. The maximum alongshore average speed was used to determine the CCC position, which reached up to 40 cm/s in front of PA and 32 cm/s in front of TO and PC, and was located around 11, 14, and 8 km offshore, respectively (Fig. 15b).

Below the CCC, both coarser grids reproduced a poleward flow adjacent to the slope and covering most of the shelf bottom layer (Fig. 1a-f), which matched well observations of the Peru-Chile UnderCurrent (PCUC) described for the region (Strub). Unlike the observed

with the CCC, the annual transport of PCUC was stronger in the HRM0 than the LRM0 (ca 0.4 fold).

The maximum poleward flow in the PCUC was located at 33°S in both coarser grids reaching -4 and -4.5 cm/s for LRM0 and HRM0, respectively, although there was a decreasing speed upstream from -2.6 to -3.6 cm/s and -2.4 to -4.3 cm/s for the same simulations (Table 3). The transport showed the same trend, where LRM0 with maximum values at 33°S and

Table 2: Seasonal difference between the LRM0, the nested HRM0 and HYCOM along the Coastal Chilean Current (CCC). The table compares the Svedrup transport (1Sv = 10^8 cm/s), the meridional current velocity (cm/s), the zonal Layer Width (LW, km) and the vertical Lower Layer (LL, meters) of the CCC. The CCC transport estimated in the HYCOM reanalysis were as follow: 30°S=0.37 Sv; 33°S = 0.09 Sv and 36°S = 0.33 Sv.

	LRM0				HRM0			
	Sv	cm/s	LW (km)	LL (m)	Sv	cm/s	LW (km)	LL (m)
30°S								
fall	0.19	5.6	51	94	0.17	4.7	78	88
winter	0.14	6.1	36	105	0.12	6.2	30	112
spring	0.25	7.4	49	106	0.34	2.2	30	73
summer	0.17	5.2	48	89	0.05	3.9	26	71
average	0.19±0.1	6.1±0.9	46±6	98±8	0.17±0.1	4.3±1.7	41±24	86±19
33°S								
fall	0.1	4.4	45	83	0.06	5.5	37	56
winter	0.2	5.2	48	126	0.3	8.7	84	110
spring	0.06	5.1	34	72	0.06	5.4	30	58
summer	0.2	8.3	44	95	0.1	7.2	47	69
average	0.14±0.1	5.7±1.8	42±6	94±23	0.13±0.1	6.7±1.6	49±24	73±25
36°S								
fall	0.3	6	63	97	0.15	3.8	65	74
winter	0.66	7.7	58	317	0.89	6.4	74	400
spring	0.7	11	63	160	0.42	8	56	135
summer	0.24	7.7	70	83	0.12	4.5	58	84
average	0.48±0.2	8.1±2.2	64±5	164±107	0.4±0.4	5.6±1.9	63±8	173±154

varying from -0.58 Sv to -0.95 Sv. Similarly, the nested HRM0 resulted in a transport of -0.91 Sv and -1.32 Sv between 30°S and 33°S, with the weaker transport of -0.7 Sv at 36°S. The spring-summer season concentrated most of the transport in both coarser grids.

The LRM0 and nested HRM0 alongshore subsurface velocities were generally weaker than those in the HYCOM reanalysis, with the largest departure observed in the northern transect (30°S), where the PCUC transport was larger by a factor of 4.9 and 3.8, respectively, especially by the offshore extension of the PCUC in HYCOM (Fig. 1g-i). While the PCUC

Table 3: Seasonal difference between the LRM0 and the nested HRM0 along the Peru-Chile Undercurrent (PCUC). The table compares the Svedrup transport (1Sv = 10^8 cm/s), the meridional current velocity (cm/s), the zonal Layer Width (LW, km) and the vertical Upper Layer (UL, m) of the PCUC. The transport estimated in the HYCOM reanalysis were as follow: 30°S= -4.42 Sv; 33°S = -1.65 Sv and 36°S = -0.53 Sv.

	LRM0				HRM0			
	Sv	cm/s	LW (km)	UL (m)	Sv	cm/s	LW (km)	UL (m)
30°S								
fall	-0.75	-3.9	57	78	-0.81	-4.3	53	76
winter	-0.63	-3.7	55	30	-0.7	-3.3	60	94
spring	-0.78	-3.4	64	46	-1.2	-5	70	64
summer	-0.8	-3.6	61	55	-0.86	-4.7	44	51
average	-0.74±0.1	-3.6±0.2	59±4	52±20	0.91±0.3	-4.3±0.7	57±11	71±18
33°S								
fall	-0.8	-3.6	61	27	-1.45	-4.8	92	24
winter	-0.5	-3.3	53	82	-0.24	-1.6	57	22
spring	-1.08	-4.5	62	34	-2	-6.1	80	20
summer	-1.4	-4.6	94	26	-1.6	-5.4	90	20
average	-0.95±0.4	-4±0.7	68±18	42±27	-1.32±0.7	-4.5±2	80±16	22±2
36°S								
fall	-0.73	-3	98	30	-0.99	-2.9	118	27
winter	-0.39	-2.2	87	75	-0.15	-1.5	84	184
spring	-0.59	-3.1	85	84	-0.41	-2.1	94	104
summer	-0.6	-2.2	103	32	-1.24	-2.9	137	31
average	-0.58±0.1	-2.6±0.5	93±8	55±28	-0.7±0.5	-2.4±0.7	108±24	87±74

width was extended within the first 100 km from shore in both coarser grids, the offshore extension in HYCOM reached nearly 200 km offshore (Fig. 1g). Another notable difference among both coarser grids was the higher salinity (34.6 psu) reached by the LRM0 and which is directly associated with the PCUC features (1a-f). Contrasting the resolutions, the HRM2 showed that, vertically, the PCUC extends between 100 to 400 meters depth, with speeds around 5 up 18 cm/s in front of Punta Curaumilla (Fig. 2c). Over the slope, the PCUC was more intense, which contrasts with the LRM0 where the flow is less intense (up 8 cm/s) and farther from the bottom. In the HRM2, the core poleward flow detaches from the slope in front of Las Cruces (Fig. 2e), where the Maipo River submarine canyon is located, decreasing its velocity compared with the downstream maximum speed reached in front of Punta Curaumilla, a pattern not reproduced in the LRM0 (Fig. 2d and f).

The most remarkable crosshore differences associated with the resolution was the nearshore forming of CBL. Here, the HRM2 showed decreasing velocities from the middle to the inner-shelf (ca. 20 km) to the shore, with a further decrease below the seasonal average at about 5 km offshore, used here to define the position of the CBL (Fig. 3). While the cross-shore velocity trends were very similar between seasons in the inner-shelf, there were seasonal differences offshore of about 18 km, where the cross-shore mean velocities were stronger in winter than in summer (Fig. 3a). The HRM2 also showed that the CCC equatorward (alongshore) flow increased rapidly from the shore to reach a maximum close to the inferred CBL position, ca. 5-7 km offshore, before decreasing again offshore until approximately 20 Km offshore, when it reached more spatially constant values towards the offshore ocean. Summer alongshore flows were slightly higher in summer than in winter within the shelf (Fig. 3c).

Thus, the cross-shore and alongshore current gradients confirm that the resolution of the HRM2 is sufficient to allow the formation of a CBL in the inner portion of the shelf. By contrast, a CBL does not form in the LRM0 (Fig. 3b, d). Although a slight decrease in alongshore velocity was seen in the LRM0 within the closest 11.5 km to the coast (16.1 to 14.5 cm/s), the coastal speeds were still higher than the summer average. To validate the performance of both coarser grids, the annual eddy kinetic energy (EKE) was compared

between the LRM0, HRM0 and satellite observations from AVISO in the same domain as LRM0 and below the AVISO resolution. Similarly, EKE changes related with the resolution increment were determinated contrasting the LRM0 and HRM2 (Table 4). The geostrophy EKE was calculated from the sea-level anomaly and using the equation (3). The based-satellite geostrophy EKE fluctuated between 22 and 115 cm^2/s^2 (Fig. 4a) within the 73° and 78°W meridional band. The spatial distribution showed two high energy centers, the

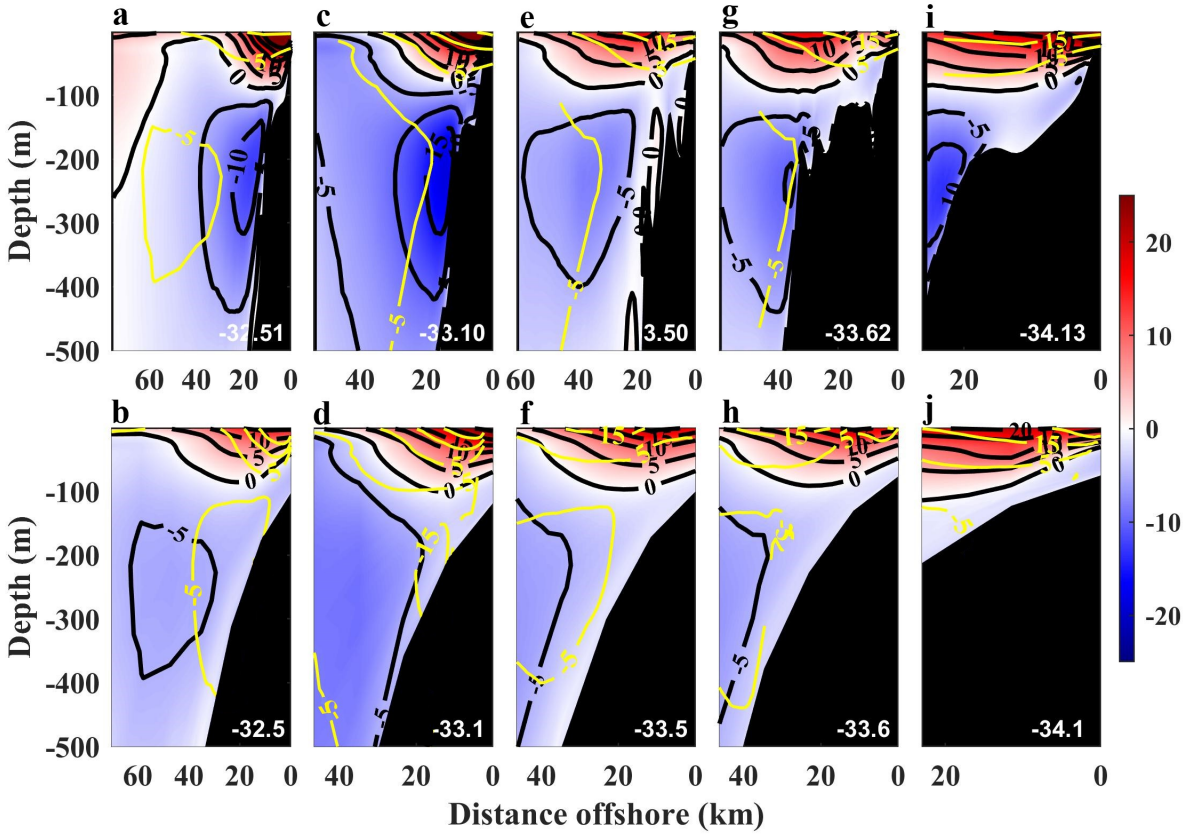

Figure 2: Alongshore currents obtained from the HRM2 (upper panels) with the LRM0 (bottom panels). The transects were located crosshore the sites of Papudo (PA, a-b), Punta Curaumilla (PC, c-d), Las Cruces (LC, e-f), Punta Toro (PT, g-h) and Topocalma (TO, i-j). The CCC (shade red) and PCUC (shade blue) were represented. In the upper (lower) panel, the black contour line represent the velocity in the HRM2 (LRM0), which have been contrasted against the yellow contour representing the current velocity in LRM0 (HRM2). Each models was compared below its own resolution.

main one sharper positioned between 28°and roughly 31°S, and a weaker one farther south between 33°-37°S. Overall, the LRM0 exhibited higher geostrophy EKE than is present in the satellite product (Fig. 4c), which ranged from 1.4 up 266 cm^2/s^2 within the same meridional band, but distributed between 28° y 34°S. The contrast between the satellite data and the HRM0 was more apparent because of the stronger geostrophy EKE in the model, which reached up 422 cm^2/s^2, concentrated mostly between 28° and 34°S (Fig. 4d)). Although, there were a broad difference between the ranges of geostrophy EKE, the average values were closer with 59.2, 86.7 and 107 cm^2/s^2 for AVISO, LRM0 and HRM0, respectively. The difference between the coarser grids reveal much sharper turbulent activity within the HRM0 than the LRM0 (Fig. 4b).

In the HRM0, the EKE appears increasing mainly inside the northern region where the nesting domains were conducted. Outside the nested domain, the southern region, and specifically near Punta Lavapie (37.2°S), the EKE was at least 100 cm^2/s^2 stronger in the LRM0 (Fig. 4b). The sharp EKE in the HRM0 may be related to a enhanced current speed or turbulent activity associated to the nesting domains inside this coarse grid. Hence, the total EKE was estimated through components of the current to solve the ageostrophy EKE and determine a positive correlation with the geostrophy EKE related with nested grid.

However, the ageostrophy EKE were fairly similar between both grids, with 12.9 $\pm$ 13.5 and 10.5 $\pm$ 15.4 cm^2/s^2 for the LRM0 and HRM0, respectively, representing the 13% and 9% of the total EKE. Inside the HRM2 domain (32°-34.5°S), the annual geostrophy EKE increased to 186 $\pm$ 41 cm^2/s^2 in the LRM0 and 368 $\pm$ 158 cm^2/s^2 in the HRM2 (Fig. 5a), where the main difference seems to form a filament towards northwesat off Punta Curaumilla (Fig. 5a). Despite, that more able energy is produced with more resolution, the HRM2 held a low ageostrophy EKE (3 $\pm$ 6% of total EKE) restricted to specific sites over the shelf, closer to the headlands and recognized as upwelling sites (i.e. Papudo, Punta Curaumilla and Punta de Toro, Fig. 5b). Meanwhile the LRM0 enhanced to 28 $\pm$ 10% the ageostrophy EKE (Table 4). The results suggest that an important amount of energy may be transfered from the shelf to the open ocean and where the higher resolution was able to capture the location of important ageostrophy circulation (i.e. Ekman transport) that contributed up

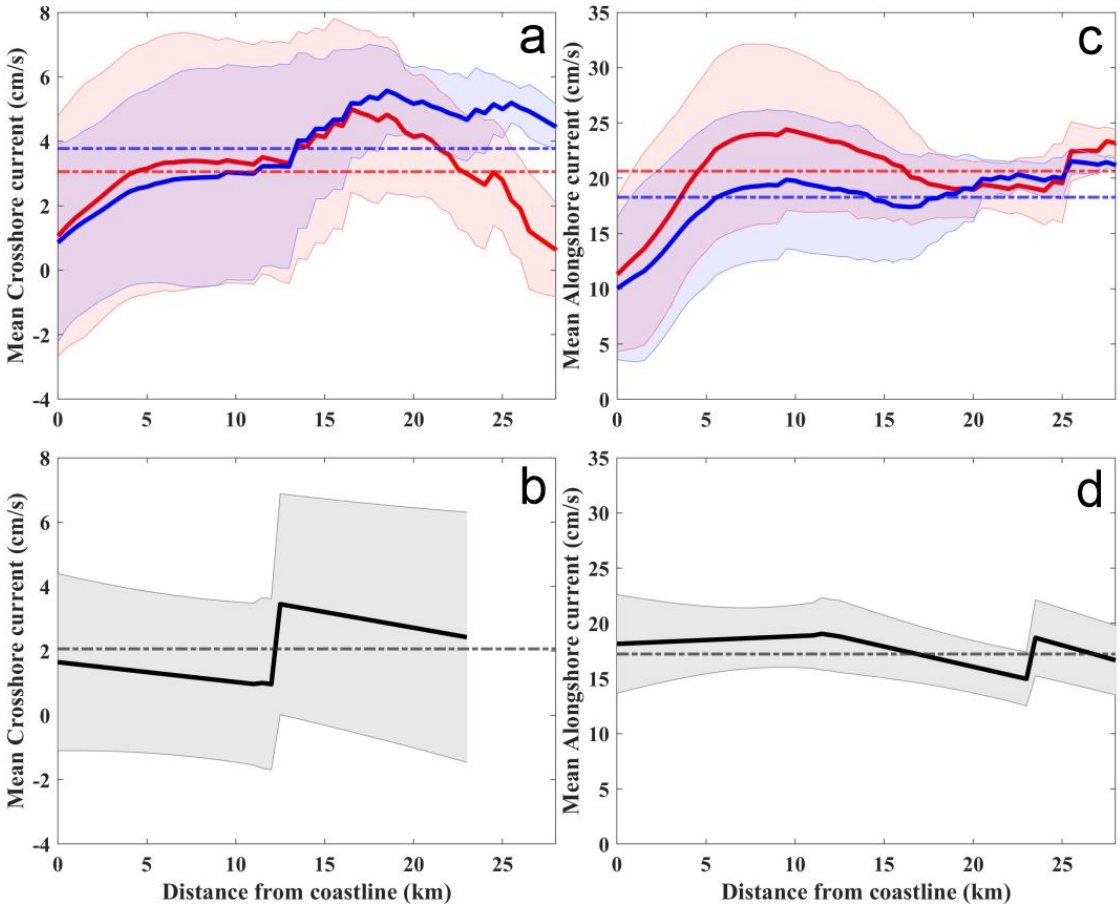

Figure 3: Coastal Boundary Layer (CBL) represented through the integrated crosshore (a, b) and alongshore (c, d) current in the HRM2 (upper panels) and LRM0 (bottom panels). The figure describe a decline in the current velocity below the seasonal average (dotted line). The blue line correspond to the winter season and the red line to the summer in the HRM2. The LRM0 only shows the summer season.

38% of the nearshore total EKE.

Another validation source compared the seasonal climatological structure of sea surface salinity (SSS) and temperature (SST) off central Chile (Fig. 10) between the LRM0 and CARS. Spatial correlation coefficients for SSS ranged from 0.94 up 0.97, while the SST varied between 0.89 and 0.94 during spring and summer, respectively. The SSS presented a standard deviation for spring and autumn close to those found in CARS observations (0.22 psu, Fig. 10a and c), while SST showed overall spatial standard deviations greater than observations, but closely similar during winter and autumn (1.2 °C, Fig. 10b and d).

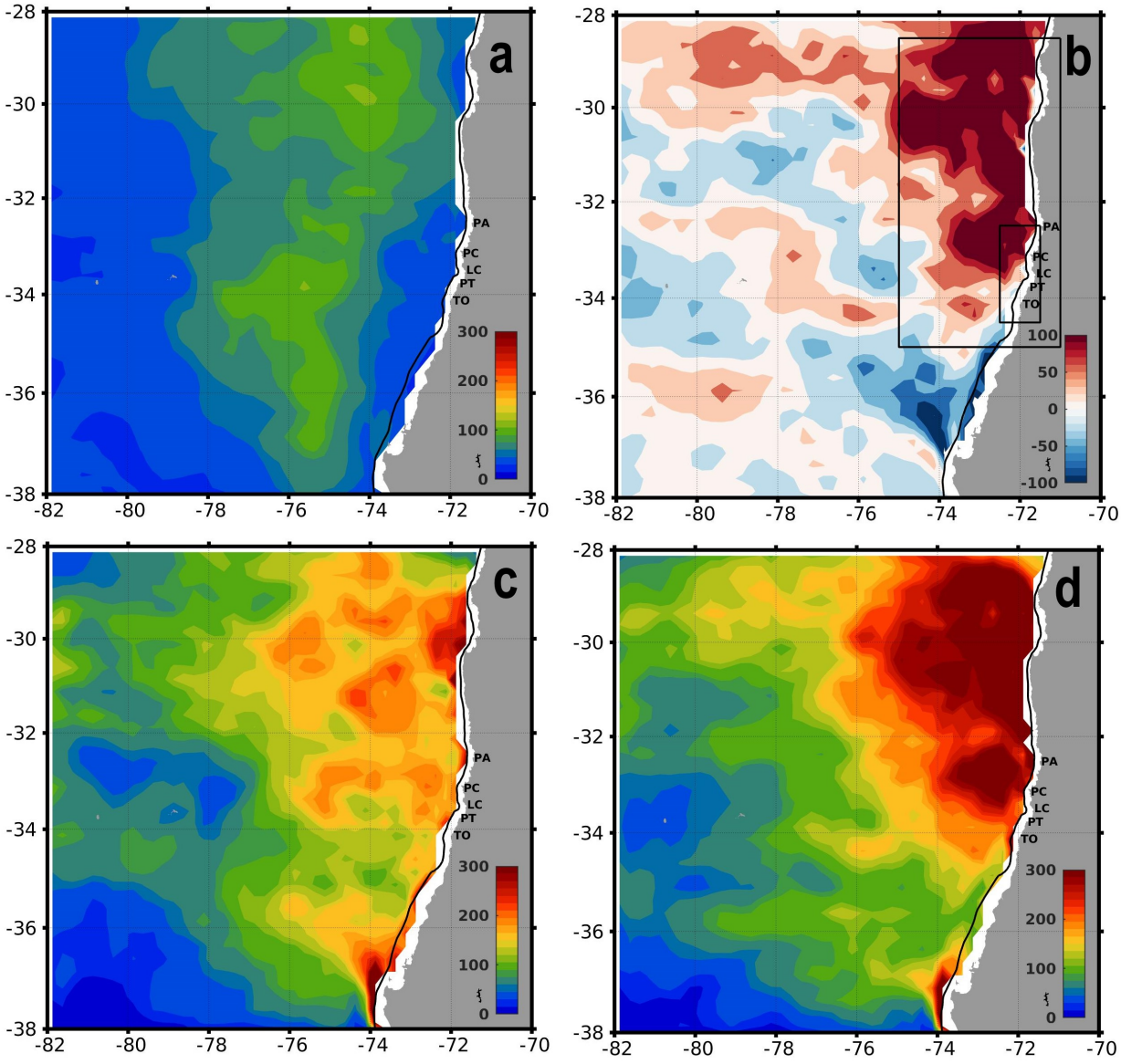

Figure 4: Annual Eddy Kinetic Energy (EKE) calculated from satellite sea-level anomaly from AVISO (2000-2014)(a) and simulated sea-level height anomaly in LRM0 (c) and HRM0 (d). Each coarse grid was previously downscaled to the AVISO resolution. The EKE difference between the nested HRM0 and LRM0 have depicted in panel b, as well as the nested domains inside HRM0 (HRM1 and HRM2), were enclosed inside the rectangles.

Moreover, the centered root-mean-square (RMS) showed that SST and SSS remained close to observations, with differences ranging between ± 0.41 to ± 0.55 °C and ± 0.05 to ± 0.09 psu, respectively. The LRM0 also exhibited good spatial coherence with observed

seasonal sea level anomaly (SLA), but with more defined sea-level structures, which rendered only a moderate spatial correlation with observations (Fig. 11a and b).

In contrast to the comparatively large differences in EKE between the LRM0 and HRM2, the other oceanographic variables (i.e. u, v, w, speed, temperature, density and the normalized relative vorticity) were seasonally described in the Table 6 and showed only small differences. Here, the water column was divided in integrated surface (0-20 m) and bottom (150-200 m) layers according with the main alongshore currents (i.e. CCC and PCUC). In the surface layer, the horizontal currents were faster in the LRM0 during the summer

Table 4: Distribution of EKE in the coarser grids (LRM0 and HRM0) contrasted with satellite observations from AVISO and the contribution of geostrophy and ageostrophy circulation to the total EKE in the LRM0 and HRM2.

	AVISO	LRM0	HRM0	HRM2
		Coarser domain and AVISO resolution		
geos-EKE				
mean	59.2	86.7	107	
SD	22.5	56.5	81.8	
range	22-115	1.4-266	1.3-422	
ageos-EKE				
mean		12.9	10.5	
SD		13.5	15.4	
range		13-94	0.3-118	
		finest domain and LRM0 resolution		
geos-EKE				
mean		186		368
SD		43.7		158
range		80-303		44-1300
ageos-EKE				
mean		78.4		11.1
SD		51.3		21.8
range		0-308		0-109

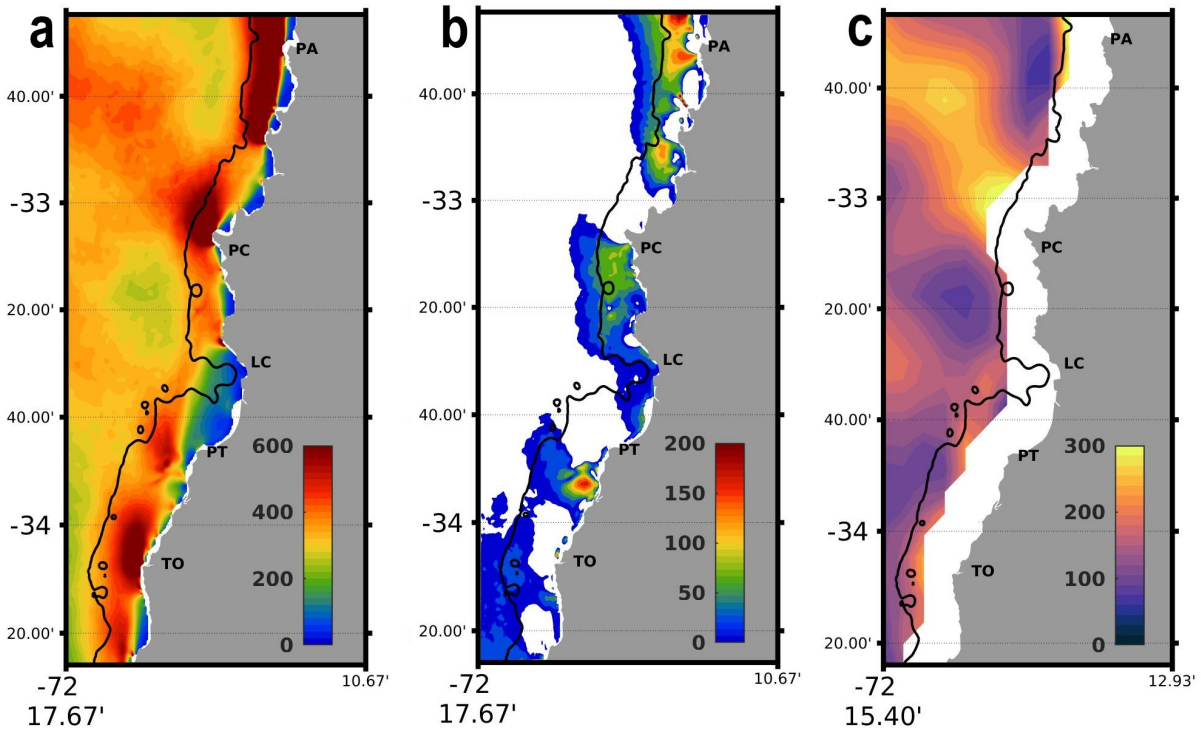

Figure 5: Annual Eddy Kinetic Energy (EKE) from the HRM2 decomposed in total EKE (a) and ageostrophic EKE (b). The panel c shows the difference between the HRM2-LRM0 associated to the total EKE. The HRM2 was downscaled to the LRM0 resolution.

(12.2 ± 4.3 cm/s) and slower during the winter (10.8 ± 5.4 cm/s) than the HRM2 (Fig. 6a-f). However, the maximum speed that reached up 24.5 cm/s in summer and up 23.9 cm/s in winter were located nearshore in the HRM2, as well as the slower speed closer to the bays (Table 6e-f). The alongshore and crosshore components of the horizontal current described the predominance of equatorward advective circulation and the seasonal Ekman transport, which are directly related with the vertical flow. Vertically, the surface alongshore current velocity was faster shoreward and the direction was predominantly equatorward in both season and model resolution (Fig 12g-l). The HRM2 showed a higher equatorward flow nearshore than the LRM0 in both seasons (up 24.1 and up 23.5 cm/s for summer and winter, respectively) (Fig 12i-l), even though in average the LRM0 was faster during the summer (12.1 ± 5.2 cm/s) but slightly lower in winter. These differences ranged in -10.1 and 8.3 cm/s in summer and -15.7 and 8.7 cm/s in winter for the HRM2 respect to the LRM0. In

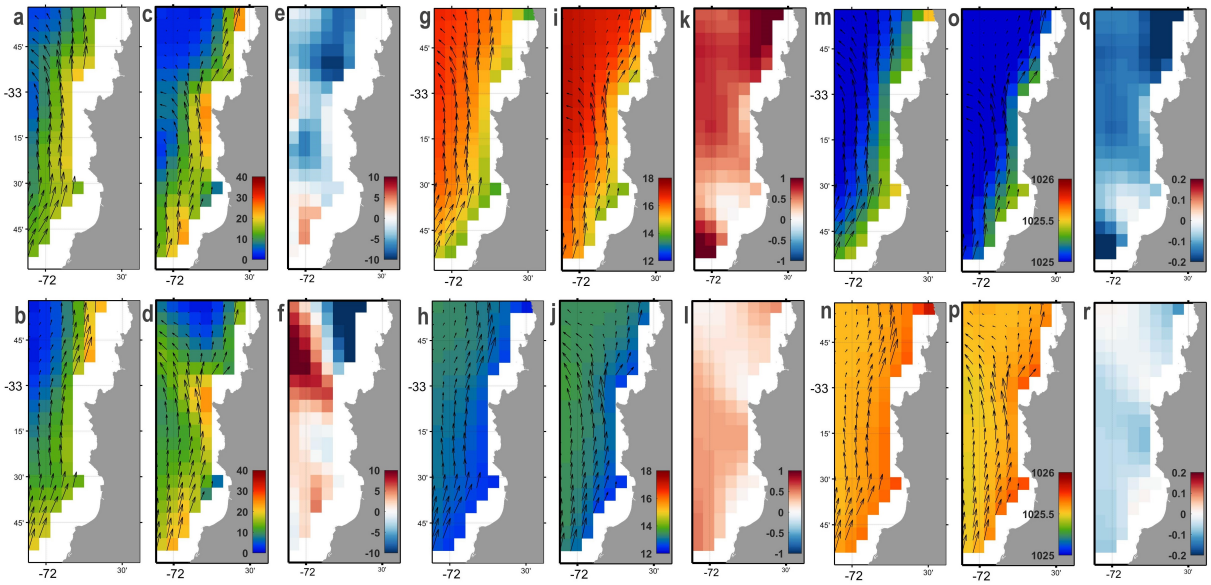

Figure 6: Seasonal average of the speed current (cm/s), SST (°C) and density (kg/m^3) in the LRM0 (a-b, g-h and m-n, respectively) and HRM2 (c-d, i-j and o-p, respectively). For difference between HRM2 and LRM0 (e-f, k-l and q-r, respectively), the positive (negative) values indicate a higher (lower) magnitude in the HRM2 than LRM0. The upper panel represents the summer season and the lower panel the winter, both integrated vertically (0-20 meters). The HRM2 was downscaled to the LRM0 resolution. The arrows describe the flow speed direction

the bottom layer, also the HRM2 was faster (-7.2 ± 2.4 cm/s) than the LRM0 (-5.6 ± 1.1 cm/s), but more close to the slope (Fig 12e), with a dominant poleward flow in summer but less strong in winter (Fig 12c-d). During summer and winter, the crosshore velocity in the surface layer showed a clear offshore transport in the HRM2 located permanently in Punta Curaumilla, which is correlated with the alongshore flow (Fig 13i-l). However, the LRM0 showed in average more offshore flow than HRM2 in summer (Table 6) and less in winter, but the higher offshore velocities were presented in the HRM2 in both season (up -7 cm/s and up -9.4 cm/s, respectively). In the bottom layer, the expected shoreward flow related to the upwelling season was lower in LRM0 (-1.1 ± 0.6 cm/s) than in HRM2 (-1.1 ± 2.1 cm/s), but in winter the maximum shoreward flow decreased in the HRM2 (3.3 to 1.9 cm/s), as should be expected for winter season, while the LRM0 increased from 0 to 2.1 cm/s since summer to winter (Fig 13a-f). The vertical flow in both coarser grids was dominated by the

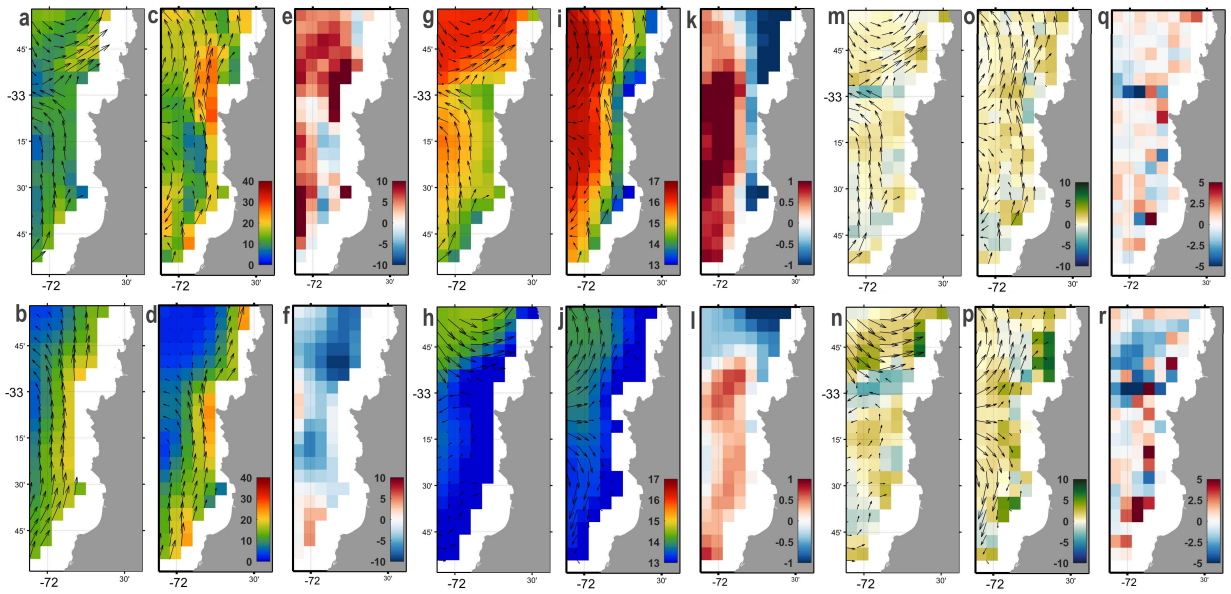

Figure 7: Mean circulation in the surface (0 - 20 meters; upper panels) and bottom layers (30 - 70 meters; lower panels), during a favorable upwelling period (16 to 27 December in nineteenth year). In order, the speed current (cm/s), SST (°C) and vertical current (m/d) in the LRM0 (a-b, g-h and m-n, respectively) and HRM2 (c,-d, i-j, and o-p, respectively). For difference between HRM2 and LRM0 (e-f, k-l and q-r, respectively), the positive (negative) values indicate a higher (lower) magnitude in the HRM2 than LRM0. The upper panel represents the summer season and the lower panel the winter. The HRM2 was downscaled to the LRM0 resolution. The arrows describe the flow speed direction.

upward flow in both season, with maximum values along nearshore and close to the slope (Fig 14a-l). During the summer, the upward flow in the surface layer was slightly higher in the HRM2 (0.4 ± 0.5 m/d) than LRM0 (0.3 ± 0.47 m/d), but the upwelling on front Punta Curaumilla was stronger in LRM0 than in the HRM2. In winter, the upward flow decreased in both simulations and showed the same average, but HRM2 keep more variance (0.2 ± 0.3 m/d, Table 6). The seasonal currents components determined almost similar velocities in both resolution, but with more variance in the HRM2. This small difference must reflect more upwelling nearshore in higher resolution. The summer and winter temperatures were higher in the HRM2 (16.2 and 13.3 °C) than the LRM0 (15.6 and 13 °C), but in the known upwelling sites (Punta Curaumilla and Punta de Toro), the temperatures were almost similar in both resolutions and seasons (Fig. 6k-l). Moreover, the thermal gradient

in the HRM2 was stronger at least in summer (Fig. 6i). Also, the more dense nearshore waters in both models specially during the summer support the upwelling occurrence, where within the LRM0, the processes seems more intense ((Fig. 6)m, o and q). However, in fact the surface colder and salty intermediate waters in the LRM0 (see Figure 1a) affected the coastal density causing a artifact. On other hand, in the bottom layer the density was the same in both resolutions without seasonal differences (Table 6). Locally, Punta Curaumilla and Punta Toro sites matched the ageostrophic EKE (Fig. 5b) and suggesting that the finer resolution intensified the Ekman transport, probably caused by the complex topography. Other sites of upwelling intensification identified in observational studies, as well as sites of weak or no upwelling, were also resolved in the HRM2.

Thereby, the difference between resolutions must be huge when a short upwelling period

Table 5: Mean circulation in the LRM0 and the HRM2 during a favorable upwelling period on front Punta Curaunmilla (see Figure 9). The HRM2 was downscaled to the LRM0 resolution. The results were calculated averaging 6 pixels on front Punta Curaumilla and integrating the upper layer (0-20m) and the lower layer (30-70m). These results were contrasted with the same variable obtained within the CBL but along the whole coast and water column (2, 10, 20, 30, 40, 50, 70) and using the own resolution for each model (see Figure 8).

	V (cm/s)	U (cm/s)	W (cm/s)	ζ /f	T (°C)
			Upper Layer		
LRM0	6.5±1.1	-1.9±5.1	-0.6±0.5	0.06±0.02	14.6±0.3
HRM2	22.6±9.5	2.2±3	0.15±1.7	0.05±0.2	14.6±0.7
			Lower Layer		
LRM0	2±1	-3.2±3	-1.7±0.9	0.004±0.02	12.7±0.2
HRM2	9.2±6.6	2±2.6	-0.2±2.7	0.07±0.07	12.9±0.4
			Whole column		
LRM0	1.7±8.8	2±4.2	2.4±3.8	-0.1±0.1	
HRM2	8.54±13.3	1.8±6.1	2.2±24.1	0.1±0.7	

is analyzed. The Figure 16 and Figure 16 depicted a variability during a favorable upwelling period (13 days) in a integrated surface (0-20 m) and bottom layer (30-70 m). Such as in the seasonal analysis, the maximun speed appeared close to Punta Curaumilla and Punta de Toro (Fig. 16c), where the nearshore flow, related to the CCC, also reached the bottom (Fig. 16d) in the HRM2. During this period, the alongshore velocity was quite stronger in HRM2 (11.3 ± 8.5 cm/s) than in LRM0 (6 ± 5.4 cm/s) in the surface layer and the temperature, which was quite similar in both resolution (15.4 ± 1°C and 15.2 ± 0.6°C, respectively) and bottom layer (13.3 ± 0.6°C and 13.3 ± 0.7°C, respectively), raised colder nearshore in the finer resolution, forming a stronger horizontal thermal gradient offshore (Fig. 16i and k). The vertical current associated with the normalized relative vorticity were spatially difficult to described in the comparative coarse resolution because apparently these act more locally. Thus, the anticyclonic (negative) vorticity must be directly related to the upward flow (upwelling) and the cyclonic vorticity with the downwelling (Fig. 16m-p). In average, the HRM2 showed higher upward velocity (0.4 ± 1.7 m/d) than the LRM0 (0.16 ± 1 m/d) and maximum upward velocities up 3.7 and 3 m/d, respectively.

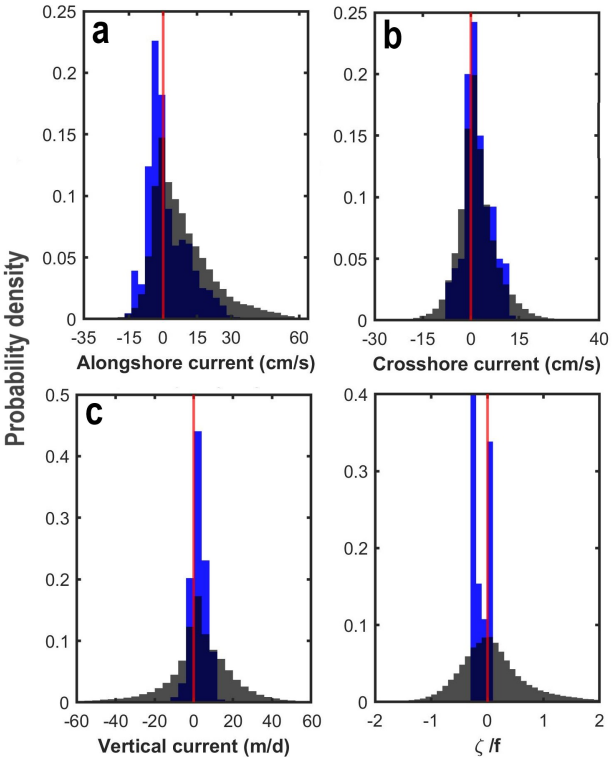

Figure 8: Relative probability (samples in a bin/total samples) of alongshore (a), crosshore (b) and vertical current (c), density (d) and relative vorticity normalized (e) during an favorable upwelling period within the CBL. The figure describes the variables for the LRM0 (blue bars) and HRM2 (gray bars). Each histogram integrated the variables through time (13 days) and depths (2, 10, 20, 30, 40, 50 and 70 m) within the CBL.

For the same period and regarding the CBL, the component of the current and the vorticity presented more variance in the HRM2 but the same average as the LRM0 when were compared using their own resolution (Fig. 8 and Table 5). The probability density of alongshore current was asymmetric in both resolution, but with most equatorward advective flow in the HRM2 varying between -30.6 to 65.3 cm/s, meanwhile, the LRM0 ranged between -15 to 31.7 cm/s (Fig 8a). Although, the variation showed extreme velocities, the averages were within expectations for CBL and lower to the values find outside the inner-shelf (8.5 $\pm$ 13.3 cm/s in the HRM2 and 1.67 $\pm$ 8.8 cm/s in the LRM0). The crosshore velocity (Fig. 8b) ranged from -25.5 to 37.2 cm/s and from -7.5 to 12.4 cm/s for the HRM2 and LRM0, respectively, but again the average were quite similar (1.8 $\pm$ 6.1 cm/s in the HRM2 and 2 $\pm$

4.2 cm/s in the LRM0). However, the vertical flow in the HRM2 was up 44 fold faster than in the LRM0, with a range between -512 and 430 m/d in HRM2 compared with the -11 to 13 m/d in the LRM0 (Fig 8c). The standard deviation was 6 fold higher in the HRM2 with 2.2 ± 24 m/d contrasting with the 2.4 ± 3.8 m/d found in the LRM0. Moreover, the relative vorticity (Fig 8d) reached values that represent submesoscale processes in the HRM2 (-5.3 to 5.7) and exceeding the planetary vorticity (Ro ¿ 1), which weren't capture by the LRM0 (-0.3 to 0.09).

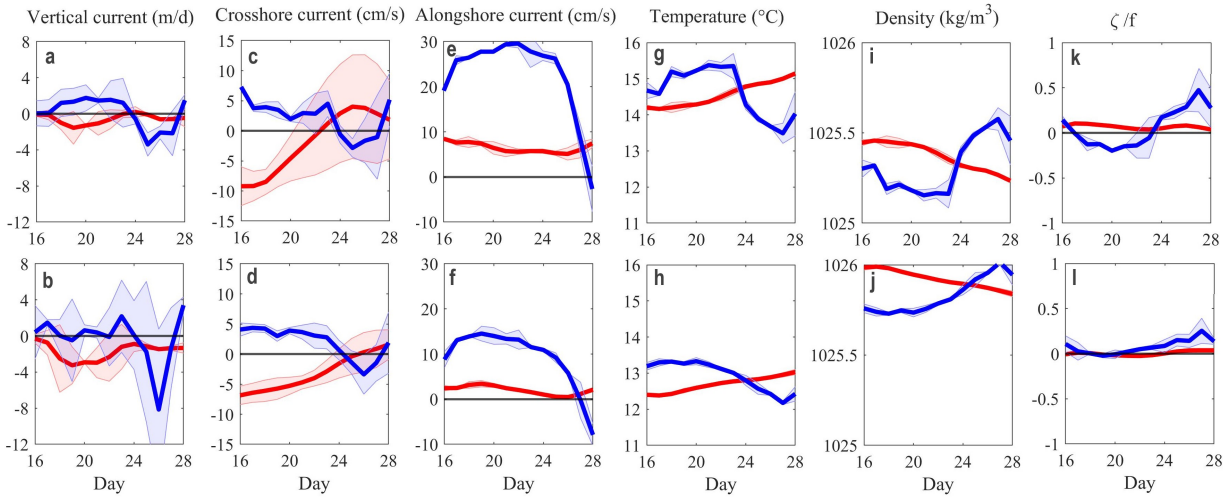

Figure 9: Time serie of mean nearshore circulation on front of Punta Curaumilla, during a favorable upwelling period between 16 to 27 December nineteenth year. The figure describe the variability of vertical (a-b), crosshore (c-d) and alongshore currents (e-f) related to changes in temperature (g-h), density (i-j) and relative vorticity normalized (k-l). The blue line represent the HRM2 and the red line the LRM0, while the upper panels to the surface layer (0 - 20 meters) and the lower panels to the bottom layer (30 - 70 meters). The standard deviation was depicted in shade color. The models were contrasted in the LRM0 resolution in an area of 15.4x23.1 km (2x3 pixels).

The differences in SST between models of different resolution noted above is linked to the significant differences in the ability of these models to resolve the coastal upwelling process. The evolution of the physical state in the surface and bottom layer in HRM2 and LRM0 during a single event of intense upwelling is illustrated in Figure 9. During the same period, the LRM0 and HRM2 responded differently to the identical wind stress forcing.

The HRM2 surface and bottom layers were accelerated to velocities of up to 30 cm/s and 15 cm/s respectively (Fig. 9e-f), simultaneously with an upward flow in both layers (Fig. 9a and b), Upon weakening of the alongshore flow 7 days into the event, an offshore flow formed consistent with Ekman transport (Fig. 9a and b), the temperature diminished (Fig. 9g and h) and the density in both surface and bottom layers increased (Fig. 9i and j). By contrast, the response of the LRM0 model to the same wind stress was weak, driving a weak alongshore current and upward flow, but with greater cross-shore transport than observed in the HRM2. The higher density and lower temperature during the time series, demonstrated that the Ekman transport started before than in the HRM2.

Discussion

Much of the variability in both the large-scale and near-shore circulation off Chile is driven by the seasonal meridional displacement of the South Pacific Anticyclone (SPA), which controls the intensification of the upwelling-favorable southwesterly wind during the austral spring-summer off central Chile (Bravo et al., 2016, Schneider et al., 2017). The climatological wind used in all resolution models allowed captures this seasonal cycle. Both coarser grids (LRM0 and HRM0) showed a good spatial correlation in SSS and SST, reproducing the corresponding seasonal alongshore gradients where colder, less salty waters predominate in the austral fall-winter, and warmer, salty waters dominate during the austral spring-summer (Sobarzo et al., 2007). The effect of seasonality over the main meridional currents was confidently reproduced by the coarser grids, increasing the transport during summer and decreasing in winter for the CCC and PCUC. Also the models reproduced the meridional gradient in the transport. Significantly difference between the LRM0 and the HRM0 weren´t observed over the CCC. However, the HRM0 had a less salty PCUC with higher transport (-0.7 $\pm$ 0.5 to -1.3 $\pm$ 0.7 Sv) and speed magnitudes (-2.4 $\pm$ 0.7 to -4.5 $\pm$ 2 cm/s). Other simulations, for the same region, have estimated the annual transport in -0.9 to -0.71 Sv (Aguirre et al., 2014), in -0.8 to -0.76 Sv (Vergara et al., 2016) and between -0.88 to -0.71 Sv (Pizarro-Koch et al., 2019). These results are closer to our results obtained from the LRM0, which early demonstrated a nesting and resolution effect able to accelerate the

flow in the HRM0.

Resolution grid differences arose more clearly when the LRM0 and HRM2 were compared. Thus, the CCC flow transported between 0.8 to 1.6 fold more water than the LRM0, meanwhile the PCUC was up 3 fold faster (0.8 to 16 cm/s) at 33°S and reached the same density as the LRM0. Similar velocities have been recorded at 30°S in the PCUC core by Shaffer et al. (up to 12.8 cm/s, Shaffer et al., 1999). Furthermore, other numerical simulations have estimated comparable speeds between 7.6 to 11.8 cm/s (Leth & Shaffer, 2001) and 10 cm/s (Vergara et al., 2016). In the finer resolution, the PCUC seems to interact more with the slope which might induce the subsurface eddy generation due to abrupt change in topography that accelerate the flow, the relative vorticity and export matter offshore (Contreras et al., 2019). However, the lower resolution bathymetry in the coarser grids avoid the acceleration flow related with the vorticity causing receding from the slope and widening of the stream.

The spatial distribution of EKE in the LRM0 resembles the Coastal Transition Zone described in Hormazabal et al (2004), a region with high mesoescale eddy activity along 29° to 39°S associated with strong and variable southerly wind stress. While satellite derived EKE identifies two EKE cores, located around 30°S and between 33 and 37°S, the LRM0 matched the 30°S core (i.e. Coquimbo Bay), but also presented at least two other local EKE maxima across 33°S (i.e. near Valparaiso Bay) and 37.2°S (i.e. along Punta Lavapie). Southern Coquimbo Bay is located close to the Punta Lengua de Vaca, a cape known by interact strongly with the equatorward flow inducing the formation of jets and eddies seaward (Shaffer et al., 1999, Hormazabal et al., 2004). In the same line, Punta Lavapie is recognized by the same ocean-land interaction southern Arauco Gulf and strong southerly winds stress, jets and eddies formation (Mesias et al., 2001, Aguirre et al., 2012). Less windy but known as an important upwelling zone is Punta Curaumilla located southern Valparaiso Bay, whose topography allow the generation of northward cold filaments (Silva & Valdenegro, 2003), which reproduced the HRM2 mostly in winter.

While increasing the horizontal resolution of the model resulted in significant improvements in the simulation of near-shore processes, it also resulted in an over-estimation of the

off-shore EKE. The reason for EKE being substantially greater than estimated from satellite altimetry may be related to the scatterometer winds used for forcing, which cannot resolve the decrease in wind speed within the first 5km offshore (Capet et al., 2014). This will tend to increase the alongshore current, Ekman transport, upwelling (Bravo et al., 2016, Astudillo et al., 2019), frontal instabilities and finally EKE (Brink, 2015, Marchesiello et al., 2003). To wit, the LRM0 reproduces a broader zone of cold and dense surface waters than HRM2, where the upwelling is restricted to some specific sites. In the LRM0 case, the absence of wind drop-off favors the upwelling by Ekman transport over Ekman pumping (Capet et al., 2004) adding more EKE to the surface ocean. In the HRM2, the sources of EKE arise from the Ekman transport that increased only locally as showed the nearshore ageostrophy EKE, probably caused by the complex topography, the augmentation of current velocities and the submesoscale circulation that drive the vertical advection through small eddy formation and relative vorticity, able to transfer energy by inverse cascade mechanism to the mesoescale circulation. Capet et al (2008), studying a toy model of upwelling determined that fine resolution below 1.5 km may increase the submesoescale circulation. The surface flow acceleration is a known result of resolution increment (Marchesiello et al., 2003) and acts as the main source of EKE, propagating the energy around the domain. Therefore, increasing the grid resolution involves an increment in EKE related to flow acceleration and submesoscale circulation that occurs during the year and whose magnitude is enough to be captured in the seasonal mean analysis.

The degree to which the observed upwelling was reproduced varied between the spatial and time resolution. Colder nearshore surface temperatures at Punta Curaumilla in HRM2, relative to LRM0, demonstrate the increased intensification of upwelling due to increased resolution, especially when the daily variability is analyzed. In fact, the warmer offshore (17°C) and colder inshore (13.5°C) temperature gradient in the HRM2 during the summer strengthened the region of baroclinic instability between 71.8 and 72.4° W, which is a source of EKE (Brink, 2016). In the HRM2, upwelling cooled near-shore SST down up 13.5°C - similar to the observations (¡14°C) reported by Silva and Valdenegro (2003), where the temperature keep low after decline the winds stress. The mean Ekman transport, calculated

as the vertical flow in the 356 km^2 varied in 533 to 627 m^3/s, a value into of moderate upwelling expected for a wind of ¡ 7 m/s. In addition to classical Ekman coastal upwelling, the interaction of the CCC with the bathymetry, especially adjacent to headlands, can cause it to branch upwelling (Leth et al., 2004, Leth & Middleton, 2004). Notably HRM2, but weak in the LRM0, a CCC branch becomes detached from the coast in front of PC during summer and winter, resembling the cold filament described by Silva and Valdenegro (2003). Over the continental shelf, Leth and Shaffer (2001) simulated a equatorward surface current velocity around 10-20 cm/s during the austral summer, estimating that the main factor responsible of meandering and eddy formation was the bathymetry and coastline variations, which may supply vorticity to the flow and sharpen the horizontal velocity shear, which then causes instabilities and the subsequent growth of meanders. Thus, the strong equatorward advection, represented in our model as a positive skewness dominating the surface circulation over the shelf, in addition with the eddy and meander formation coupled to the Ekman transport, together should be feeding the mesoescale EKE increment.

Despite the along-shore flow acceleration seen in the HRM2, the horizontal currents were less sensitive to the change in resolution, than the vertical speed and normalized relative vorticity. Marchesiello et al (2003) modeling the large-scale circulation in the California Current System determined an insensitivity of the horizontal currents to the model resolution through seasonal averages, indicating that the main difference ocurred shoreward over the EKE and sea level anomaly. Also, Capet et al (Capet et al.) concluded the same low sensitivity of horizontal current to the resolution increment but regardless the first 80 km of coast offshore. Similarly, Zhong and Bracco (2013), comparing two resolution models (1 and 5 km) forced by diurnal winds over the Gulf of Mexico, finding no difference in the horizontal velocities but mainly in vorticity where the coarser grid reproduced the same structures smoothed. However, the emergence of a CBL in the HRM2 allowed to capture more variance in the horizontal current within the km of offshore but keeping the mean. Evenly, the normalized relative vorticity showed a large variance with more positive skewness to the cyclonic eddies over the shelf, meanwhile, the vertical flow showed a Gaussian distribution with large variance in the HRM2. The variance was up 2, 3, 38, and 42 folds higher in the

HRM2 than the LRM0 over CBL into the innershelf.

The decline in the integrated velocity of horizontal current coincides with the cross-shore observations in the Northeast Pacific shelf carried-out by Nickols et al (2012, 2012), which suggest a logaritmic speed decay relative to the coastline distance even when existed topographic and bathymetric difference between the sampled sites. The HRM2 reproduces a CBL on average within the first 5 km offshore over the continental shelf. The lateral boundary layer is caused by the transferal of lateral and bottom stress by eddy viscosity (Nickols et al.). The resolution of the LRM0 is too low to resolve this process. The CBL is known to impact essential ecological processes such as larval dispersal and metapopulation connectivity of rocky shore communities by allowing the larval retention and accumulation across the inner-shelf, facilitating the self-recruitment (Nickols et al., 2012). This higher retention within the first kilometers from the coastline has been evaluated by Dauhajre et al.(2017), suggesting that in models with resolution over 1 km, the retention results of an underestimation of the vertical and horizontal speed currents that conform filaments and fronts, which would increase the exchange within the CBL compared to grid resolutions under 100 m. On the other hand, Brandini et al, (2017), correlated simulations with X-frecuency radar inside the CBL, which showed submesoscale eddies which would be associated to the interaction between the current with the bathymetrical complexity and where the vorticity generation trigger a processes of current attenuation.

We have presented clear evidence that using fine grid of at least 1 km of resolution, together with a detailed bathymetry, allows to improve the simulation of small-scale processes, such as submesoescale turbulence, ageostrophy circulation and the CBL. Even though the finer resolution intensified of the upwelling, limiting the spatial extension seen in the coarser grids. The horizontal current velocity increased most variance within the CBL, keeping the average and the more relevant changes were associated to the vorticity and vertical current enhanced by the topographical flow interaction. Despite the high EKE, our model provides a good simulation of CBL, impossible to reproduce in lower resolution, and the nearshore mixing processes, turning it in a valuable tool to applied in ecological larval dispersal studies. Thus, the application of high resolution models for open ocean questions

seems inadequate on the horizontal scale, unless a near-shore problem regarding the CBL been addressed. The variability capture by the high resolution grids could even increase when a high resolution bathymetry is adopted as initial condition, which have been suggested in other studies (Saldías & Allen, 2020). The ecological application of high resolution models is then recommended in studies applied in nearshore species.

Acknowledgements

This study was financed by a Regular FONDECYT-1200636 to SAN. Additonal support was provided by the Powered@NLHPC: supercomputing infrastructure of the NLHPC (ECM-02), for whihc we are most grateful. Juan Faúndez was funded by a Doctoral Scholarship of CONICYT (Comisión Nacional de Investigación Científica y Tecnológica, Ministry of Education, Chile), which also supported doctoral internships at the Laboratoire de Mathematiques (LAMA) at Universite de Savoie Mont Blanc. We wish to thank Dr. Héctor Sepúlveda and Dr. Florian Lemarié for their early helpful comments in the CROCO configuration. The (Marine Energy Research and Innovation Center, MERIC made possible this international collaboration.

References

Aguirre, C., Garreaud, R. D., & Rutllant, J. A. (2014). Surface ocean response to synoptic-scale variability in wind stress and heat fluxes off south-central Chile. *Dynamics of Atmospheres and Oceans*, *65*, 64–85. URL: http://www.sciencedirect.com/science/article/pii/S0377026513000699. doi:10.1016/j.dynatmoce.2013.11.001.

Aguirre, C., Pizarro, , Strub, P. T., Garreaud, R., & Barth, J. A. (2012). Seasonal dynamics of the near-surface alongshore flow off central Chile. *Journal of Geophysical Research: Oceans*, *117*. URL: http://doi.wiley.com/10.1029/2011JC007379. doi:10.1029/2011JC007379.

Aiken, C. M., Castillo, M. I., & Navarrete, S. A. (2008). A simulation of the Chilean Coastal Current and associated topographic upwelling near Valparaíso, Chile. *Continental Shelf Research*, *28*, 2371–2381. URL: http://www.sciencedirect.com/science/article/pii/S0278434308001994. doi:10.1016/j.csr.2008.05.006.

Aiken, C. M., Navarrete, S. A., Castillo, M. I., & Castilla, J. C. (2007). Along-shore larval dispersal kernels in a numerical ocean model of the central Chilean coast. *Marine Ecology Progress Series*, *339*, 13–24. URL: https://www.int-res.com/abstracts/meps/v339/p13-24/. doi:10.3354/meps339013.

Aiken, C. M., Navarrete, S. A., & Pelegrí, J. L. (2011). Potential changes in larval dispersal and alongshore connectivity on the central Chilean coast due to an altered wind climate. *Journal of Geophysical Research: Biogeosciences*, *116*. URL: https://agupubs.pericles-prod.literatumonline.com/doi/abs/10.1029/2011JG001731. doi:https://doi.org/10.1029/2011JG001731. _eprint: https://agupubs.onlinelibrary.wiley.com/doi/pdf/10.1029/2011JG001731.

Astudillo, O., Dewitte, B., Mallet, M., Rutllant, J. A., Goubanova, K., Frappart, F., Ramos, M., & Bravo, L. (2019). Sensitivity of the Near-Shore Oceanic Circulation Off Central Chile to Coastal Wind Profiles Characteristics. *Journal of Geophysical Research: Oceans*, *124*, 4644–4676. URL: https://agupubs.onlinelibrary.wiley.com/doi/abs/10.1029/2018JC014051. doi:10.1029/2018JC014051. _eprint: https://agupubs.onlinelibrary.wiley.com/doi/pdf/10.1029/2018JC014051.

Bani, R., Marleau, J., Fortin, M.-J., Daigle, R. M., & Guichard, F. (2021). Dynamic larval dispersal can mediate the response of marine metapopulations to multiple climate change impacts. *Oikos*, *130*, 989–1000. URL: https://onlinelibrary.wiley.com/doi/abs/10.1111/oik.07760. doi:10.1111/oik.07760. _eprint: https://onlinelibrary.wiley.com/doi/pdf/10.1111/oik.07760.

Brandini, C., Taddei, S., Doronzo, B., Fattorini, M., Costanza, L., Perna, M., Serafino, F., & Ludeno, G. (2017). Turbulent behaviour within a coastal boundary layer, observations and modelling at the Isola del Giglio. *Ocean Dynamics*, *67*, 1163–1178. URL: https://doi.org/10.1007/s10236-017-1080-1. doi:10.1007/s10236-017-1080-1.

Bravo, L., Ramos, M., Astudillo, O., Dewitte, B., & Goubanova, K. (2016). Seasonal variability of the Ekman transport and pumping in the upwelling system off central-northern Chile (30° S) based on a high-resolution atmospheric regional model (WRF). *Ocean Science*, *12*, 1049–1065. URL: https://www.ocean-sci.net/12/1049/2016/os-12-1049-2016-discussion.html. doi:https://doi.org/10.5194/os-12-1049-2016.

Brink, K. (2016). Cross-Shelf Exchange. *Annual Review of Marine Science*, *8*, 59–78. URL: https://doi.org/10.1146/annurev-marine-010814-015717. doi:10.1146/annurev-marine-010814-015717. _eprint: https://doi.org/10.1146/annurev-marine-010814-015717.

Brink, K. H. (2003). Coastal-Trapped Waves and Wind-Driven Currents Over the Continental Shelf. URL: https://www.annualreviews.org/doi/abs/10.1146/annurev.fl.23.010191.002133. doi:10.1146/annurev.fl.23.010191.002133.

Capet, X., McWilliams, J. C., Molemaker, M. J., & Shchepetkin, A. F. (2008). Mesoscale to Submesoscale Transition in the California Current System. Part II: Frontal Processes. *J.*

Phys. Oceanogr., *38*, 44–64. URL: https://journals.ametsoc.org/jpo/article/38/1/44/10895/Mesoscale-to-Submesoscale-Transition-in-the. doi:10.1175/2007JPO3672.1. Publisher: American Meteorological Society.

Capet, X. J., Marchesiello, P., & McWilliams, J. C. (2004). Upwelling response to coastal wind profiles. *Geophysical Research Letters*, *31*. URL: https://agupubs.onlinelibrary.wiley.com/doi/abs/10.1029/2004GL020123. doi:10.1029/2004GL020123.

Carton, J. A., & Giese, B. S. (2008). A Reanalysis of Ocean Climate Using Simple Ocean Data Assimilation (SODA). *Monthly Weather Review*, *136*, 2999–3017. URL: https://journals.ametsoc.org/view/journals/mwre/136/8/2007mwr1978.1.xml. doi:10.1175/2007MWR1978.1. Publisher: American Meteorological Society Section: Monthly Weather Review.

Chaigneau, A., & Pizarro, O. (2005). Eddy characteristics in the eastern South Pacific. *Journal of Geophysical Research: Oceans*, *110*. URL: https://agupubs.onlinelibrary.wiley.com/doi/abs/10.1029/2004JC002815. doi:10.1029/2004JC002815. _eprint: https://agupubs.onlinelibrary.wiley.com/doi/pdf/10.1029/2004JC002815.

Chavez, F. P., & Messié, M. (2009). A comparison of Eastern Boundary Upwelling Ecosystems. *Progress in Oceanography*, *83*, 80–96. URL: http://www.sciencedirect.com/science/article/pii/S0079661109000998. doi:10.1016/j.pocean.2009.07.032.

Connolly, T. P., Hickey, B. M., Geier, S. L., & Cochlan, W. P. (2010). Processes influencing seasonal hypoxia in the northern California Current System. *J Geophys Res*, *115*, C03021–C03021. URL: https://pubmed.ncbi.nlm.nih.gov/20463844. doi:10.1029/2009JC005283.

Contreras, M., Pizarro, O., Dewitte, B., Sepulveda, H. H., & Renault, L. (2019). Subsurface Mesoscale Eddy Generation in the Ocean off Central Chile. *Journal of Geophysical Research: Oceans*, *124*, 5700–5722. URL: https://agupubs.onlinelibrary.wiley.com/doi/abs/10.1029/2018JC014723. doi:10.1029/2018JC014723. _eprint: https://agupubs.onlinelibrary.wiley.com/doi/pdf/10.1029/2018JC014723.

Correa-Ramirez, M. A., Hormazabal, S. E., & Morales, C. E. (2012). Spatial patterns of annual and interannual surface chlorophyll-a variability in the Peru–Chile Current System. *Progress in Oceanography*, *92-95*, 8–17. URL: http://www.sciencedirect.com/science/article/pii/S0079661111000620. doi:10.1016/j.pocean.2011.07.008.

Correa-Ramirez, M. A., Hormazábal, S., & Yuras, G. (2007). Mesoscale eddies and high chlorophyll concentrations off central Chile (29°–39°S). *Geophysical Research Letters*, *34*. URL: https://agupubs.onlinelibrary.wiley.com/doi/abs/10.1029/2007GL029541. doi:10.1029/2007GL029541. _eprint: https://agupubs.onlinelibrary.wiley.com/doi/pdf/10.1029/2007GL029541.

Cowen, R. K., & Sponaugle, S. (2009). Larval Dispersal and Marine Population Connectivity. *Annual Review of Marine Science*, *1*, 443–466. URL: https://doi.org/10.1146/

annurev.marine.010908.163757. doi:10.1146/annurev.marine.010908.163757. _eprint: https://doi.org/10.1146/annurev.marine.010908.163757.

Dauhajre, D. P., McWilliams, J. C., & Renault, L. (2019). Nearshore Lagrangian Connectivity: Submesoscale Influence and Resolution Sensitivity. *Journal of Geophysical Research: Oceans*, *124*, 5180–5204. URL: https://agupubs.onlinelibrary.wiley.com/doi/abs/10.1029/2019JC014943. doi:https://doi.org/10.1029/2019JC014943. _eprint: https://agupubs.onlinelibrary.wiley.com/doi/pdf/10.1029/2019JC014943.

Dauhajre, D. P., McWilliams, J. C., & Uchiyama, Y. (2017). Submesoscale Coherent Structures on the Continental Shelf. *J. Phys. Oceanogr.*, *47*, 2949–2976. URL: https://journals.ametsoc.org/doi/full/10.1175/JPO-D-16-0270.1. doi:10.1175/JPO-D-16-0270.1.

Debreu, L., Marchesiello, P., Penven, P., & Cambon, G. (2012). Two-way nesting in split-explicit ocean models: Algorithms, implementation and validation. *Ocean Modelling*, *49-50*, 1–21. URL: http://www.sciencedirect.com/science/article/pii/S1463500312000480. doi:10.1016/j.ocemod.2012.03.003.

Dewitte, B., Ramos, M., Echevin, V., Pizarro, O., & duPenhoat, Y. (2008). Vertical structure variability in a seasonal simulation of a medium-resolution regional model of the Eastern South Pacific. *Progress in Oceanography*, *79*, 120–137. URL: http://www.sciencedirect.com/science/article/pii/S0079661108001675. doi:10.1016/j.pocean.2008.10.014.

Gibson, R. N., Atkinson, R. J. A., & Gordon, J. D. M. (2007). *Oceanography and Marine Biology: An Annual Review, Volume 45*. CRC Press. Google-Books-ID: bb5dEUANTp0C.

Gruber, N., Lachkar, Z., Frenzel, H., Marchesiello, P., Münnich, M., McWilliams, J. C., Nagai, T., & Plattner, G.-K. (2011). Eddy-induced reduction of biological production in eastern boundary upwelling systems. *Nature Geoscience*, *4*, 787–792. URL: https://www.nature.com/articles/ngeo1273. doi:10.1038/ngeo1273. Number: 11 Publisher: Nature Publishing Group.

Harrison, C., Siegel, D., & Mitarai, S. (2013). Filamentation and eddyeddy interactions in marine larval accumulation and transport. *Marine Ecology Progress Series*, *472*, 27–44. URL: http://www.int-res.com/abstracts/meps/v472/p27-44/. doi:10.3354/meps10061.

Hormazabal, S., Shaffer, G., & Leth, O. (2004). Coastal transition zone off Chile. *Journal of Geophysical Research: Oceans*, *109*. URL: https://agupubs.onlinelibrary.wiley.com/doi/abs/10.1029/2003JC001956. doi:https://doi.org/10.1029/2003JC001956. _eprint: https://agupubs.onlinelibrary.wiley.com/doi/pdf/10.1029/2003JC001956.

Kirincich, A. R., & Barth, J. A. (2009). Alongshelf Variability of Inner-Shelf Circulation along the Central Oregon Coast during Summer. *Journal of Physical Oceanography*, *39*, 1380–1398. URL: https://journals.ametsoc.org/view/journals/phoc/39/6/2008jpo3760.1.xml. doi:10.1175/2008JPO3760.

1. Publisher: American Meteorological Society Section: Journal of Physical Oceanography.

Largier, J. L. (2003). Considerations in estimating larval dispersal distances from oceanographic data. *Ecological Applications*, *13*, 71–89. URL: https://esajournals.onlinelibrary.wiley.com/doi/full/10.1890/1051-0761%282003%29013%5B0071%3ACIELDD%5D2.0.CO%3B2. doi:10.1890/1051-0761(2003)013[0071:CIELDD]2.0.CO;2.

Largier, J. L. (2020). Upwelling Bays: How Coastal Upwelling Controls Circulation, Habitat, and Productivity in Bays. *Annual Review of Marine Science*, *12*, 415–447. URL: https://doi.org/10.1146/annurev-marine-010419-011020. doi:10.1146/annurev-marine-010419-011020. _eprint: https://doi.org/10.1146/annurev-marine-010419-011020.

Lentz, S. J., & Fewings, M. R. (2012). The Wind- and Wave-Driven Inner-Shelf Circulation. *Annual Review of Marine Science*, *4*, 317–343. URL: https://doi.org/10.1146/annurev-marine-120709-142745. doi:10.1146/annurev-marine-120709-142745.

Letelier, J., Pizarro, O., & Nuñez, S. (2009). Seasonal variability of coastal upwelling and the upwelling front off central Chile. *Journal of Geophysical Research: Oceans*, *114*. URL: https://agupubs.onlinelibrary.wiley.com/doi/abs/10.1029/2008JC005171. doi:10.1029/2008JC005171.

Leth, O., & Middleton, J. F. (2004). A mechanism for enhanced upwelling off central Chile: Eddy advection. *Journal of Geophysical Research: Oceans*, *109*. URL: https://agupubs.onlinelibrary.wiley.com/doi/abs/10.1029/2003JC002129. doi:10.1029/2003JC002129. _eprint: https://agupubs.onlinelibrary.wiley.com/doi/pdf/10.1029/2003JC002129.

Leth, O., & Shaffer, G. (2001). A numerical study of the seasonal variability in the circulation off central Chile. *Journal of Geophysical Research: Oceans*, *106*, 22229–22248. URL: https://agupubs.onlinelibrary.wiley.com/doi/abs/10.1029/2000JC000627. doi:https://doi.org/10.1029/2000JC000627. _eprint: https://agupubs.onlinelibrary.wiley.com/doi/pdf/10.1029/2000JC000627.

Leth, O., Shaffer, G., & Ulloa, O. (2004). Hydrography of the eastern South Pacific Ocean: results from the Sonne 102 cruise, May–June 1995. *Deep Sea Research Part II: Topical Studies in Oceanography*, *51*, 2349–2369. URL: http://www.sciencedirect.com/science/article/pii/S0967064504001663. doi:10.1016/j.dsr2.2004.08.009.

Liu, X., & Levine, N. M. (2016). Enhancement of phytoplankton chlorophyll by submesoscale frontal dynamics in the North Pacific Subtropical Gyre. *Geophys Res Lett*, *43*, 1651–1659. doi:10.1002/2015GL066996.

Mahadevan, A. (2016). The Impact of Submesoscale Physics on Primary Productivity of Plankton. *Annual Review of Marine Science*, *8*, 161–184. URL: https://doi.org/10.1146/annurev-marine-010814-015912. doi:10.1146/annurev-marine-010814-015912. _eprint: https://doi.org/10.1146/annurev-marine-010814-015912.

Marchesiello, P., McWilliams, J. C., & Shchepetkin, A. (2003). Equilibrium Structure and Dynamics

of the California Current System. *J. Phys. Oceanogr.*, *33*, 753–783. URL: https://journals.ametsoc.org/jpo/article/33/4/753/68530/Equilibrium-Structure-and-Dynamics-of-the. doi:10.1175/1520-0485(2003)33<753:ESADOT>2.0.CO;2. Publisher: American Meteorological Society.

McWilliams, J. C. (2003). Diagnostic Force Balance and its Limits. In O. U. Velasco Fuentes, J. Sheinbaum, & J. Ochoa (Eds.), *Nonlinear Processes in Geophysical Fluid Dynamics: A tribute to the scientific work of Pedro Ripa* (pp. 287–303). Dordrecht: Springer Netherlands. URL: https://doi.org/10.1007/978-94-010-0074-1_17. doi:10.1007/978-94-010-0074-1_17.

McWilliams, J. C. (2016). Submesoscale currents in the ocean. *Proceedings of the Royal Society A: Mathematical, Physical and Engineering Sciences*, *472*, 20160117. URL: https://royalsocietypublishing.org/doi/10.1098/rspa.2016.0117. doi:10.1098/rspa.2016.0117. Publisher: Royal Society.

Medel, C., Parada, C., Morales, C. E., Pizarro, O., Ernst, B., & Conejero, C. (2018). How biophysical interactions associated with sub- and mesoscale structures and migration behavior affect planktonic larvae of the spiny lobster in the Juan Fernández Ridge: A modeling approach. *Progress in Oceanography*, *162*, 98–119. URL: http://www.sciencedirect.com/science/article/pii/S0079661116302373. doi:10.1016/j.pocean.2018.02.017.

Mesias, J. M., Matano, R. P., & Strub, P. T. (2003). Dynamical analysis of the upwelling circulation off central Chile. *Journal of Geophysical Research: Oceans*, *108*. URL: https://agupubs.onlinelibrary.wiley.com/doi/abs/10.1029/2001JC001135. doi:10.1029/2001JC001135. _eprint: https://agupubs.onlinelibrary.wiley.com/doi/pdf/10.1029/2001JC001135.

Mitarai, S., Siegel, D. A., & Winters, K. B. (2008). A numerical study of stochastic larval settlement in the California Current system. *Journal of Marine Systems*, *69*, 295–309. URL: http://www.sciencedirect.com/science/article/pii/S0924796307000590. doi:10.1016/j.jmarsys.2006.02.017.

Morgan, S. G. (2014). Behaviorally Mediated Larval Transport in Upwelling Systems. URL: https://www.hindawi.com/journals/aocean/2014/364214/. doi:https://doi.org/10.1155/2014/364214 iSSN: 2356-6809 Pages: e364214 Publisher: Hindawi Volume: 2014.

Morgan, S. G., Fisher, J. L., Miller, S. H., McAfee, S. T., & Largier, J. L. (2009). Nearshore larval retention in a region of strong upwelling and recruitment limitation. *Ecology*, *90*, 3489–3502. URL: https://esajournals.onlinelibrary.wiley.com/doi/full/10.1890/08-1550.1. doi:10.1890/08-1550.1.

Nickols, K., Miller, S., Gaylord, B., Morgan, S., & Largier, J. (2013). Spatial differences in larval abundance within the coastal boundary layer impact supply to shoreline habitats. *Marine Ecology Progress Series*, *494*, 191–203. doi:10.3354/meps10572.

Nickols, K. J., Gaylord, B., & Largier, J. L. (2012). The coastal boundary layer: predictable current structure decreases alongshore transport and alters scales of dispersal. *Marine Ecology Progress Series*, *464*, 17–35.

URL: https://www.int-res.com/abstracts/meps/v464/p17-35/. doi:10.3354/meps09875.

Nickols, K. J., White, J. W., Largier, J. L., Gaylord, B., Mooij, A. E. W. M., & Bronstein, E. J. L. (2015). Marine Population Connectivity: Reconciling Large-Scale Dispersal and High Self-Retention. *The American Naturalist*, *185*, 196–211. URL: https://www.jstor.org/stable/10.1086/679503. doi:10.1086/679503.

Oerder, V., Colas, F., Echevin, V., Codron, F., Tam, J., & Belmadani, A. (2015). Peru-Chile upwelling dynamics under climate change. *Journal of Geophysical Research: Oceans*, *120*, 1152–1172. URL: https://agupubs.onlinelibrary.wiley.com/doi/abs/10.1002/2014JC010299. doi:https://doi.org/10.1002/2014JC010299. _eprint: https://agupubs.onlinelibrary.wiley.com/doi/pdf/10.1002/2014JC010299.

Ospina-Alvarez, A., Weidberg, N., Aiken, C. M., & Navarrete, S. A. (2018). Larval transport in the upwelling ecosystem of central Chile: The effects of vertical migration, developmental time and coastal topography on recruitment. *Progress in Oceanography*, *168*, 82–99. URL: http://www.sciencedirect.com/science/article/pii/S0079661117300800. doi:10.1016/j.pocean.2018.09.016.

Parada, C., Colas, F., Soto-Mendoza, S., & Castro, L. (2012). Effects of seasonal variability in across- and alongshore transport of anchoveta (Engraulis ringens) larvae on model-based pre-recruitment indices off central Chile. *Progress in Oceanography*, *92-95*, 192–205. URL: https://www.sciencedirect.com/science/article/pii/S0079661111000693. doi:10.1016/j.pocean.2011.07.015.

Penven, P., Echevin, V., Pasapera, J., Colas, F., & Tam, J. (2005). Average circulation, seasonal cycle, and mesoscale dynamics of the Peru Current System: A modeling approach. *Journal of Geophysical Research: Oceans*, *110*. URL: https://agupubs.onlinelibrary.wiley.com/doi/abs/10.1029/2005JC002945. doi:https://doi.org/10.1029/2005JC002945. _eprint: https://agupubs.onlinelibrary.wiley.com/doi/pdf/10.1029/2005JC002945.

Penven, P., Roy, C., Brundrit, G. B., Verdiere, A. C. d., Freon, P., Johnson, A. S., Lutjeharms, J. R. E., & Shillington, F. A. (2001). A regional hydrodynamic model of upwelling in the Southern Benguela : research letter. *South African Journal of Science*, *97*, 472–475. URL: https://journals.co.za/content/sajsci/97/11-12/EJC97265. Publisher: Academy of Science for South Africa (ASSAf).

Pitcher, G. C., Probyn, T. A., du Randt, A., Lucas, A. J., Bernard, S., Evers-King, H., Lamont, T., & Hutchings, L. (2014). Dynamics of oxygen depletion in the nearshore of a coastal embayment of the southern Benguela upwelling system. *Journal of Geophysical Research: Oceans*, *119*, 2183–2200. URL: https://agupubs.onlinelibrary.wiley.com/doi/abs/10.1002/2013JC009443. doi:10.1002/2013JC009443.

Pizarro-Koch, M., Pizarro, O., Dewitte, B., Montes, I., Ramos, M., Paulmier, A., & Garçon, V. (2019). Seasonal Variability of the Southern Tip of the Oxygen Minimum Zone in the Eastern South Pacific (30°-38°S): A Modeling Study. *Journal of Geophysical Research: Oceans*, *124*, 8574–8604. URL: https://agupubs.onlinelibrary.wiley.com/doi/abs/10.1029/2019JC015201. doi:10.1029/2019JC015201.

_eprint: https://agupubs.onlinelibrary.wiley.com/doi/pdf/10.1029/2019JC015201.

Risien, C. M., & Chelton, D. B. (2008). A Global Climatology of Surface Wind and Wind Stress Fields from Eight Years of QuikSCAT Scatterometer Data. *Journal of Physical Oceanography*, *38*, 2379–2413. URL: https://journals.ametsoc.org/view/journals/phoc/38/11/2008jpo3881.1.xml. doi:10.1175/2008JPO3881.1. Publisher: American Meteorological Society Section: Journal of Physical Oceanography.

Rutllant, J. A., Rosenbluth, B., & Hormazabal, S. (2004). Intraseasonal variability of wind-forced coastal upwelling off central Chile (30°S). *Continental Shelf Research*, *24*, 789–804. URL: http://www.sciencedirect.com/science/article/pii/S0278434304000354. doi:10.1016/j.csr.2004.02.004.

Saldías, G. S., & Allen, S. E. (2020). The Influence of a Submarine Canyon on the Circulation and Cross-Shore Exchanges around an Upwelling Front. *Journal of Physical Oceanography*, *50*, 1677–1698. URL: https://journals.ametsoc.org/view/journals/phoc/50/6/JPO-D-19-0130.1.xml. doi:10.1175/JPO-D-19-0130.1. Publisher: American Meteorological Society Section: Journal of Physical Oceanography.

Schneider, W., Donoso, D., Garcés-Vargas, J., & Escribano, R. (2017). Water-column cooling and sea surface salinity increase in the upwelling region off central-south Chile driven by a poleward displacement of the South Pacific High. *Progress in Oceanography*, *151*, 38–48. URL: https://www.sciencedirect.com/science/article/pii/S0079661116300325. doi:10.1016/j.pocean.2016.11.004.

Shaffer, G., Hormazabal, S., Pizarro, O., & Ramos, M. (2004). Circulation and variability in the Chile Basin. *Deep Sea Research Part I: Oceanographic Research Papers*, *51*, 1367–1386. URL: http://www.sciencedirect.com/science/article/pii/S0967063704000974. doi:10.1016/j.dsr.2004.05.006.

Shaffer, G., Hormazabal, S., Pizarro, O., & Salinas, S. (1999). Seasonal and interannual variability of currents and temperature off central Chile. *Journal of Geophysical Research: Oceans*, *104*, 29951–29961. URL: https://agupubs.onlinelibrary.wiley.com/doi/abs/10.1029/1999JC900253. doi:https://doi.org/10.1029/1999JC900253. _eprint: https://agupubs.onlinelibrary.wiley.com/doi/pdf/10.1029/1999JC900253.

Shaffer, G., Salinas, S., Pizarro, O., Vega, A., & Hormazabal, S. (1995). Currents in the deep ocean off Chile (30°S). *Deep Sea Research Part I: Oceanographic Research Papers*, *42*, 425–436. URL: http://www.sciencedirect.com/science/article/pii/0967063795998236. doi:10.1016/0967-0637(95)99823-6.

Shchepetkin, A. F., & McWilliams, J. C. (2005). The regional oceanic modeling system (ROMS): a split-explicit, free-surface, topography-following-coordinate oceanic model. *Ocean Modelling*, *9*, 347–404. URL: http://www.sciencedirect.com/science/article/pii/S1463500304000484. doi:10.1016/j.ocemod.2004.08.002.

Silva, N., & Valdenegro, A. (2003). Evolución de un evento de surgencia frente a punta Curau-

milla, Valparaíso. *Investigaciones marinas*, *31*, 73–89. URL: https://scielo.conicyt.cl/scielo.php?script=sci_abstract&pid=S0717-71782003000200007&lng=es&nrm=iso&tlng=es. doi:10.4067/S0717-71782003000200007. Publisher: Escuela de Ciencias del Mar. Pontificia Universidad Católica de Valparaíso.

Sobarzo, M., Bravo, L., Donoso, D., Garcés-Vargas, J., & Schneider, W. (2007). Coastal upwelling and seasonal cycles that influence the water column over the continental shelf off central Chile. *Progress in Oceanography*, *75*, 363–382. URL: http://www.sciencedirect.com/science/article/pii/S0079661107001577. doi:10.1016/j.pocean.2007.08.022.

Soufflet, Y., Marchesiello, P., Lemarié, F., Jouanno, J., Capet, X., Debreu, L., & Benshila, R. (2016). On effective resolution in ocean models. *Ocean Modelling*, *98*, 36–50. URL: http://www.sciencedirect.com/science/article/pii/S1463500315002401. doi:10.1016/j.ocemod.2015.12.004.

Strub, P. T. (1998). Coastal ocean circulation off western South America. *The global coastal ocean. Regional studies and syntheses*, (pp. 273–315). Publisher: Wiley.

Strub, P. T., Combes, V., Shillington, F. A., & Pizarro, O. (2013). Chapter 14 - Currents and Processes along the Eastern Boundaries. In G. Siedler, S. M. Griffies, J. Gould, & J. A. Church (Eds.), *International Geophysics* (pp. 339–384). Academic Press volume 103 of *Ocean Circulation and Climate*. URL: http://www.sciencedirect.com/science/article/pii/B9780123918512000143. doi:10.1016/B978-0-12-391851-2.00014-3.

Strub, P. T., Mesias, J. M., & James, C. (1995). Altimeter observations of the Peru-Chile countercurrent. *Geophysical Research Letters*, *22*, 211–214. URL: https://agupubs.onlinelibrary.wiley.com/doi/abs/10.1029/94GL02807. doi:10.1029/94GL02807. _eprint: https://agupubs.onlinelibrary.wiley.com/doi/pdf/10.1029/94GL02807.

Sun, D., Bracco, A., Barkan, R., Berta, M., Dauhajre, D., Molemaker, M. J., Choi, J., Liu, G., Griffa, A., & McWilliams, J. C. (2020). Diurnal Cycling of Submesoscale Dynamics: Lagrangian Implications in Drifter Observations and Model Simulations of the Northern Gulf of Mexico. *Journal of Physical Oceanography*, *50*, 1605–1623. URL: https://journals.ametsoc.org/view/journals/phoc/50/6/JPO-D-19-0241.1.xml. doi:10.1175/JPO-D-19-0241.1. Publisher: American Meteorological Society Section: Journal of Physical Oceanography.

Tapia, F. J., Navarrete, S. A., Castillo, M., Menge, B. A., Castilla, J. C., Largier, J., Wieters, E. A., Broitman, B. L., & Barth, J. A. (2009). Thermal indices of upwelling effects on inner-shelf habitats. *Progress in Oceanography*, *83*, 278–287. URL: http://www.sciencedirect.com/science/article/pii/S0079661109000949. doi:10.1016/j.pocean.2009.07.035.

Thiel, M., Macaya, E., Acuña, E., Arntz, W., Bastias, H., Brokordt, K., Camus, P., Castilla, J., Castro, L., Cortes, M., Dumont, C., Escribano, R., Fernandez, M., Gajardo, J., Gaymer, C., Gomez, I.,

Gonzalez, A., Gonzalez, H., Haye, P., Illanes, J.-E., Iriarte, J., Lancellotti, D., Luna-Jorquera, G., Luxoro, C., Manriquez, P., Marin, V., Muñoz, P., Navarrete, S., Perez, E., Poulin, E., Sellanes, J., Sepulveda, H., Stotz, W., Tala, F., Thomas, A., Vargas, C., Vasquez, J., & Vega, A. (2007). The Humboldt Current System of Northern and Central Chile: Oceanographic Processes, Ecological Interactions And Socioeconomic Feedback. In *Oceanography and Marine Biology* (pp. 195–344). CRC Press volume 20074975. URL: http://www.crcnetbase.com/doi/abs/10.1201/9781420050943.ch6. doi:10.1201/9781420050943.ch6 series Title: Oceanography and Marine Biology - An Annual Review.

Vergara, O. A., Echevín, V., Sepúlveda, H. H., Colas, F., & Quiñones, R. A. (2016). Modelling the seasonal dynamics of the Peru-Chile Undercurrent off Central Chile (30–40°S). *Continental Shelf Research*, *123*, 61–79. URL: https://linkinghub.elsevier.com/retrieve/pii/S0278434316301789. doi:10.1016/j.csr.2016.04.001.

White, J. W., Carr, M., Caselle, J., Washburn, L., Woodson, C. B., Palumbi, S., Carlson, P., Warner, R., Menge, B., Barth, J., Blanchette, C., Raimondi, P., & Milligan, K. (2019). Connectivity, Dispersal, and Recruitment: Connecting Benthic Communities and the Coastal Ocean. *Oceanog*, *32*, 50–59. URL: https://tos.org/oceanography/article/connectivity-dispersal-and-recruitment-connecting-benthic-communities-and. doi:10.5670/oceanog.2019.310.

Zhong, Y., & Bracco, A. (2013). Submesoscale impacts on horizontal and vertical transport in the Gulf of Mexico. *Journal of Geophysical Research: Oceans*, *118*, 5651–5668. URL: https://agupubs.onlinelibrary.wiley.com/doi/abs/10.1002/jgrc.20402. doi:https://doi.org/10.1002/jgrc.20402. _eprint: https://agupubs.onlinelibrary.wiley.com/doi/pdf/10.1002/jgrc.20402.

884 ## Supplementary information

885 ### 1. Taylor Diagrams

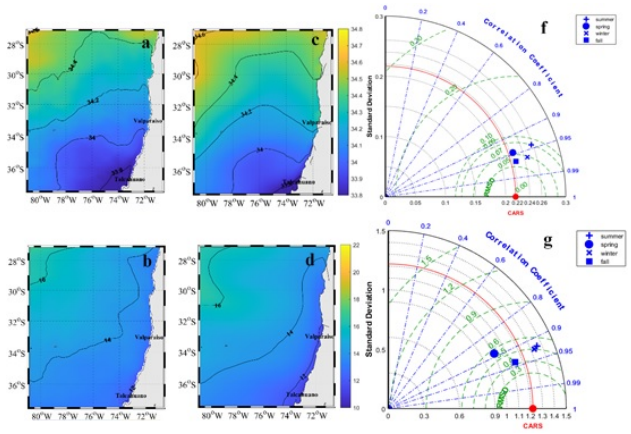

Figure 10: Sea surface temperature (SST) and salinity (SSS) during fall in the LRM0 (a and b) and observations from CARS (c and d), respectively. The Taylor diagram The Taylor diagram (c) compared the seasonal climatology of SST (f) and SSS (g) from the LRM0 with CARS observations, through the spatial correlation coefficient (dashed blue line), standard deviation (dotted black line), and the root mean square deviation (RMSD, dashed green line). The red line denote the standard deviation for the observations.

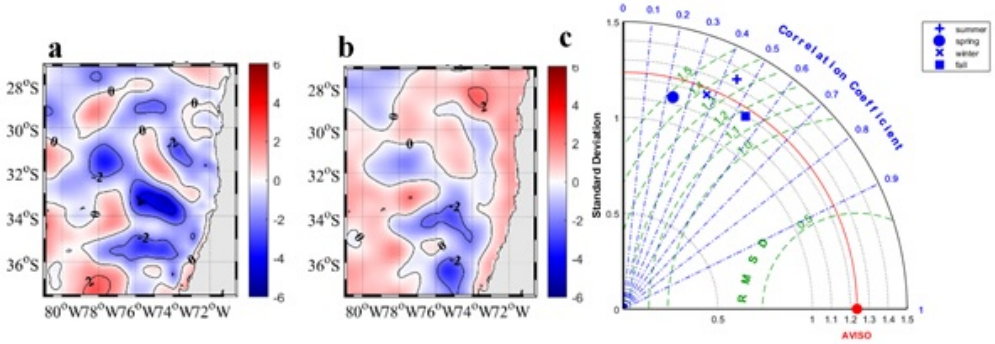

Figure 11: Annual sea-level anomaly calculated in the LRM0 (a) and satellite observation from AVISO (b). The Taylor diagram (c) compared the seasonal climatology of LRM0 with AVISO, through the spatial correlation coefficient (dashed blue line), standard deviation (dotted black line), and the root mean square deviation (RMSD, dashed green line). The red line denote the standard deviation for the observations.

886 The Taylor diagram (Fig. 11c) showed that the spatial correlation between the LRM0
887 and observations was lowest in spring (0.23) and maximum in autumn (0.54). The stan-

dard deviation values indicated that the LRM0 captures an essential fraction of the spatial variability observed in SLA (± 1.23 cm), especially during winter and autumn (± 1.2 cm), while the RMSD of the LRM0 was greater (± 1.4 to ± 1.1 cm) than the satellite anomalies (Fig. 11c).

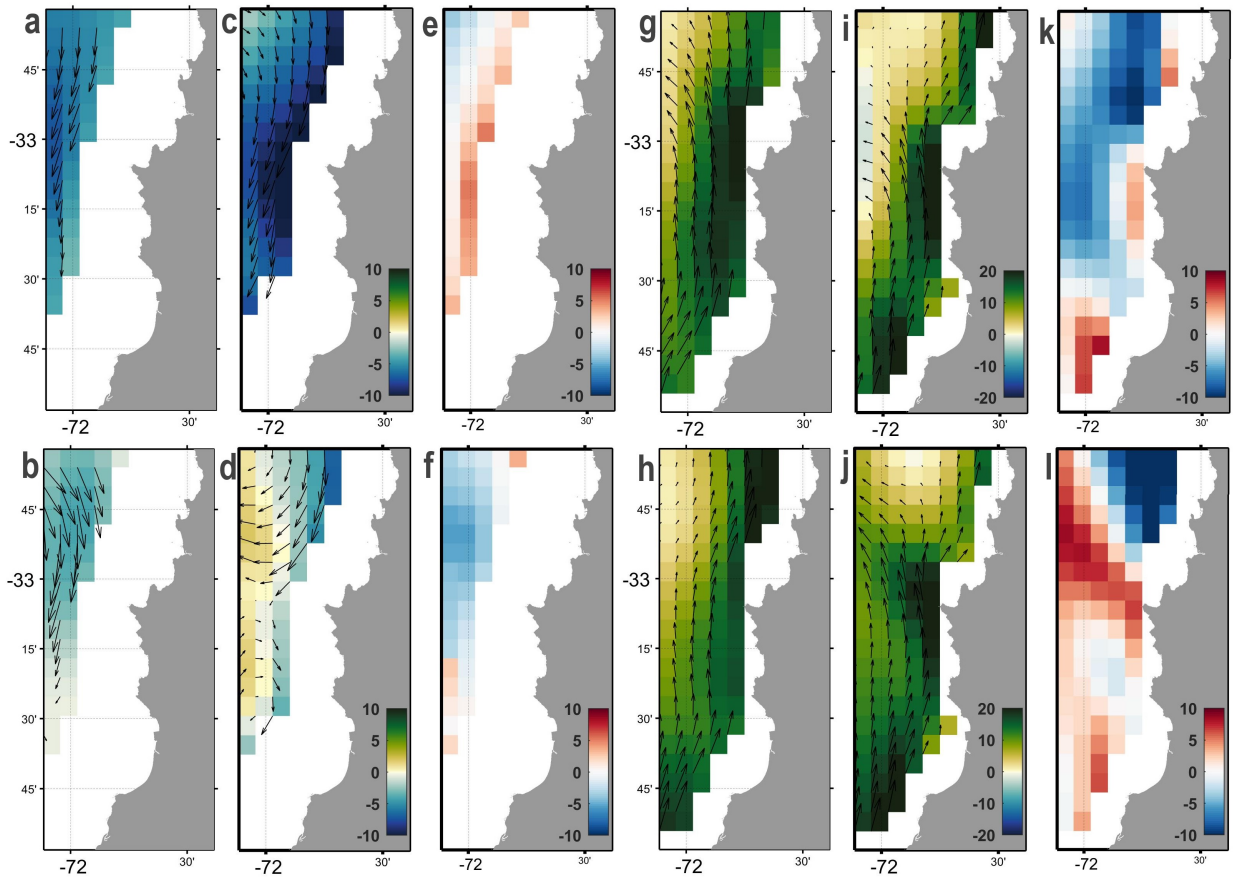

Figure 12: Seasonal average of alongshore current (cm/s) in bottom (a-f) and surface layers (g-l) integrated vertically (150-200 meters and 0-20 meters, respectively) during summer (upper panels) and winter (bottom panels). The figure compares the HRM2 (c-d and i-j) downscaled to the LRM0 (a-b and g-h) resolution. For difference between HRM2 and LRM0 (e-f and k-l), the positive (negative) values indicate a higher (lower) speed in the HRM2 than LRM0. The arrows depicts the flow speed direction.

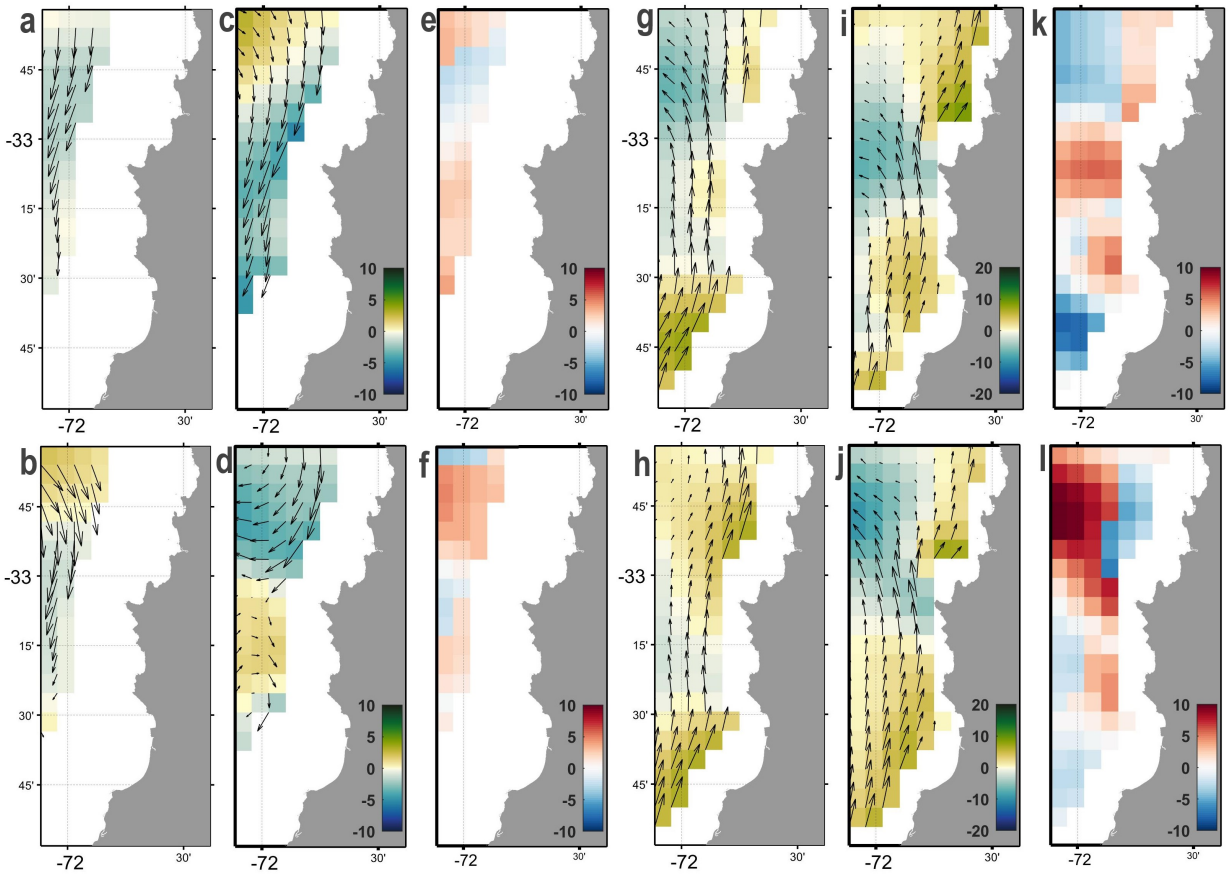

Figure 13: Seasonal crosshore current (cm/s) in bottom (a-f) and surface layers (g-l) integrated vertically (150-200 meters and 0-20 meters, respectively) during summer (upper panels) and winter (bottom panels). The figure compares the HRM2 (c-d and i-j) downscaled to the LRM0 (a-b and g-h) resolution. For difference between HRM2 and LRM0 (e-f and k-l), the positive (negative) values indicate a higher (lower) speed in the HRM2 than LRM0. The arrows depicts the flow speed direction.

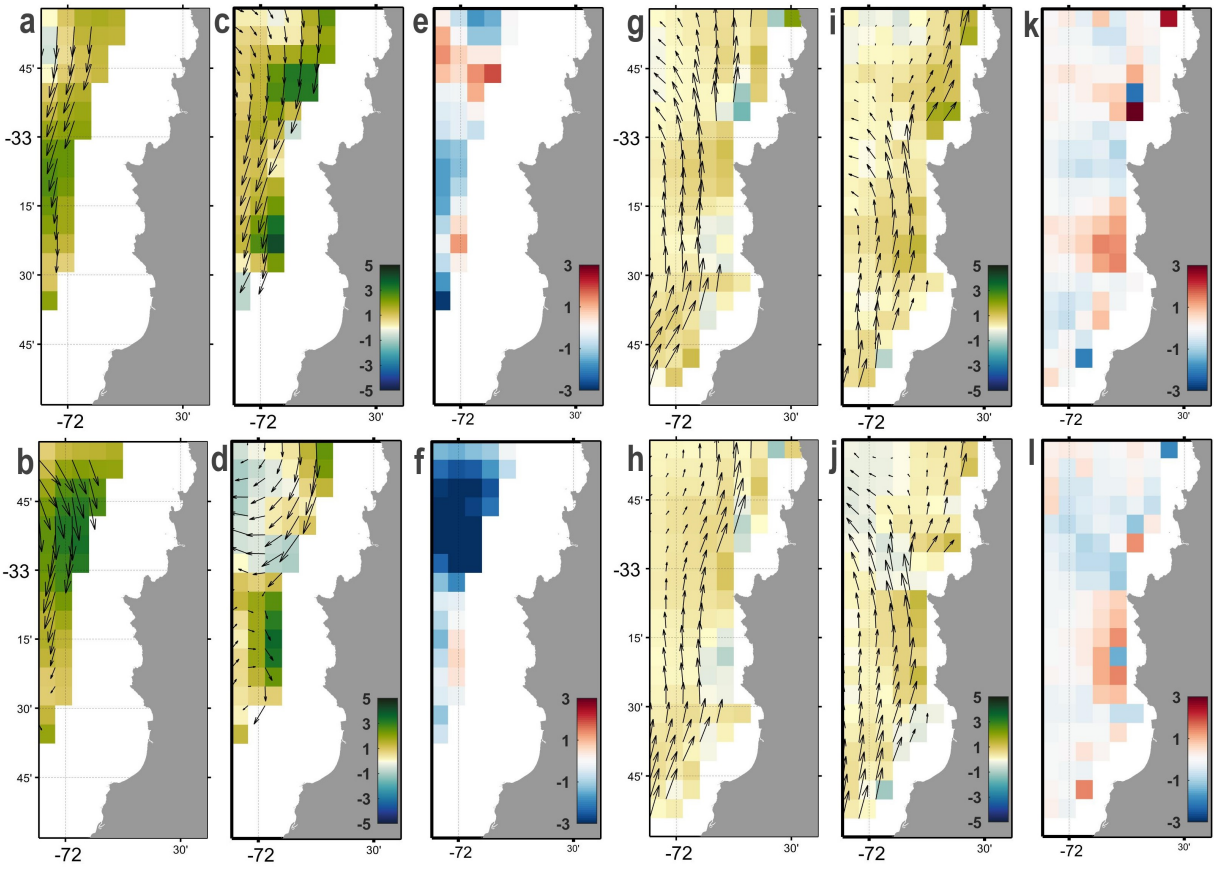

Figure 14: Seasonal average of vertical current (m/d) in bottom (a-f) and surface layers (g-l) integrated vertically (150-200 meters and 0-20 meters, respectively) during summer (upper panels) and winter (bottom panels). The figure compares the HRM2 (c-d and i-j) downscaled to the LRM0 (a-b and g-h) resolution. For difference between HRM2 and LRM0 (e-f and k-l), the positive (negative) values indicate a higher (lower) speed in the HRM2 than LRM0. The arrows depicts the flow speed direction.

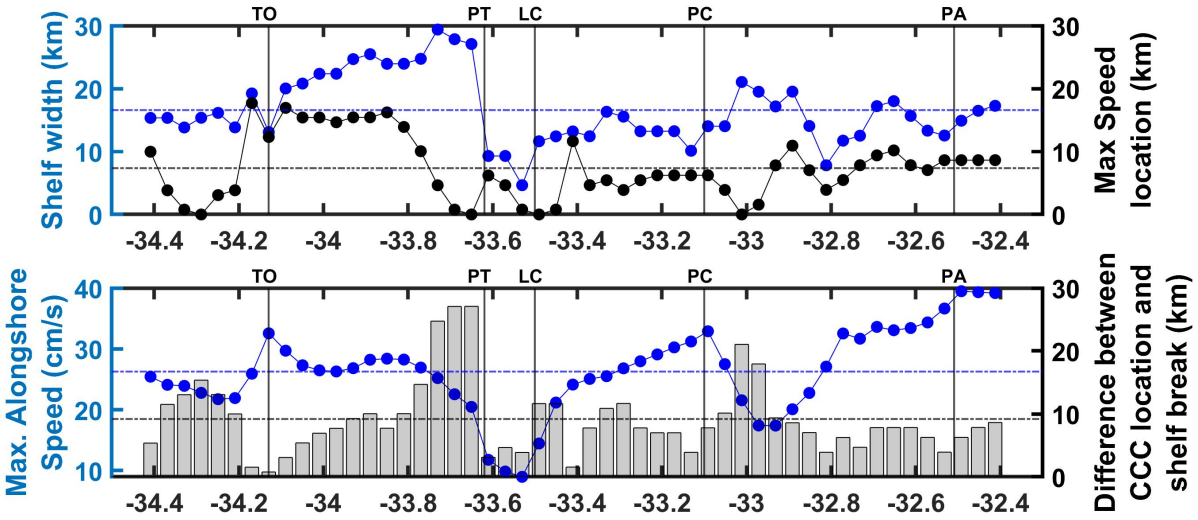

Figure 15: Upstream description of the CCC along the coastline and on front the sites TO, PT, LC, PC and PA (vertical black lines) within the HRM2. The upper panel identified the offshore location of maximum speed of CCC (black dots) and determine its distance with the shelf break (blue dots). The lower panel, The distance between the CCC and the shelf break (bars) associated with the maximun velocity of CCC. The horizontal dashed lines indicate the mean values.

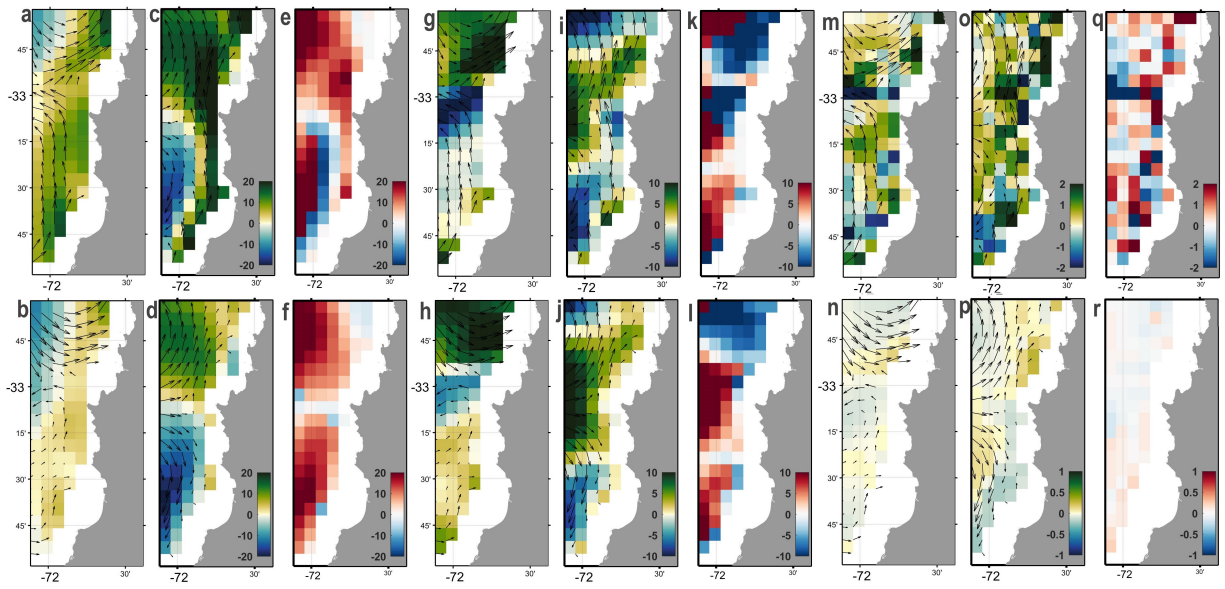

Figure 16: Mean circulation in the surface (0 - 20 meters; upper panels) and bottom layers (30 - 70 meters; lower panels), during a favorable upwelling period (16 to 27 December in nineteenth year). In order, the alongshore (cm/s) and crosshore current (cm/s) and the relative vorticity normalized (ζ/f) in the LRM0 (a-b, g-h and m-n, respectively) and HRM2 (c,-d, i-j, and o-p, respectively). For difference between HRM2 and LRM0 (e-f, k-l and q-r, respectively), the positive (negative) values indicate a higher (lower) magnitude in the HRM2 than LRM0. The upper panel represent the summer season and the lower panel the winter. The HRM2 was downscaled to the LRM0 resolution. The arrows describe the flow speed direction.

Table 6: Mean circulation in the LRM0 and the HRM2 in summer, winter and annually. The HRM2 was downscaled to the LRM0 resolution. The season were integrating the upper layer (0-20m) and the lower layer (150-200m).

	V (cm/s)	U (cm/s)	W (m/d)	Speed (cm/s)	T (°C)	Density (kg/m^3)	ζ/f
	Summer Integrated 0-20 m						
LRM0							
Mean	12.1	-0.6	0.3	12.2	15.6	1025.1	-0.06
SD	5.2	3.6	0.47	4.3	0.7	0.1	0.04
Range	1.2-22.2	-6.8-7.3	-1.6-2.1	3.8-20.6	13.8-16.6	1024.9-1025.5	-0.12-0.04
HRM2							
Mean	9.3	0.2	0.4	10.5	16.2	1025	-0.06
SD	7.3	3.4	0.5	6.5	0.8	0.2	0.07
Range	-2.2-24.1	-7-8.6	-0.8-1.9	1.8-24.5	14.2-17.3	1024.4-1024.8	-0.23-0.15
	Summer Integrated 150-200 m						
LRM0							
Mean	-5.6	-1.1	1.4	5.7	10.6	1027.1	-0.01
SD	1.1	0.6	0.8	1.0	0.03	0	0.01
range	-7.3- -3.2	-1.9-0	-0.5-2.6	3.3-7.6	10.5-10.6	1027.1	-0.03-0.01
HRM2							
Mean	-7.3	-1.1	1.3	7.7	10.3	1027.1	0.04
SD	2.4	2.1	1.1	2.4	0.03	0	0.02
Range	-12.5-1.3	-5.2-3.3	-0.8-4.1	3.5-10.4	10.3-10.4	1027-1027.1	0.01-0.09
	Winter Integrated 0-20 m						
LRM0							
Mean	11.3	1.6	0.2	10.8	13	1025.6	-0.05
SD	5.5	2.3	0.3	5.4	0.3	0.1	0.03
Range	0.9-21.8	-2.1-6.5	-1.2-1	1.8-22.7	12.2-13.4	1025.5-1025.8	-0.12-0.001
HRM2							
Mean	11.2	-0.3	0.2	12	13.3	1025.6	-0.02
SD	5.6	3.7	0.4	5.3	0.3	0.10	0.07
Range	-0.7-23.5	-9.4-7	-1.1-1.3	1.2-23.9	12.5-13.6	1025.5-1025.7	-0.15-0.18
	Winter Integrated 150-200 m						
LRM0							
Mean	-2.7	0	2	3	10.5	1027.1	0.01
SD	1.2	1	0.7	1.1	0.1	0	0.01
Range	-4.2- -0.4	-1.3-2.1	0.8-3.3	0.6-4.2	10.4-10.6	1027.1	-0.02-0.03
HRM2							
Mean	-1.3	-1.3	0.6	3	10.2	1027.1	0.04
SD	2.3	1.7	1.1	1.6	0.1	0	0.03
Range	-6.9-1.9	-4.2-1.9	-1.0-3.5	0.8-7.3	10.1-10.3	1027.1	-0.03-0.09
	Annual Integrated 0-20 m						
LRM0							
Mean	10.3	0.4	0.3	10	14.2	1025.4	-0.05
SD	5	2.3	0.4	4.7	0.5	0.1	0.02
Range	-0.3-18.5	-3.2-6	-1.1-1.4	1.7-19.1	12.9-14.8	1025.3-1025.7	-0.10-0.02
HRM2							
Mean	7.5	0.7	0.4	8.4	14.7	1025.3	-0.05
SD	6.1	2.7	0.3	5.6	0.5	0.1	0.06
Range	-0.7-22.6	-3.7-9.1	-0.7-1.7	1.7-23.2	13.3-15.3	1025.2-1025.6	-0.21-0.21
	Annual Integrated 150-200 m						
LRM0							
Mean	-4.	6 -0.6	1.8	4.8	10.5	1027.1	0
SD	1.1	0.9	0.6	1.1	0	0	0.01
Range	-5.8- -2.3	-2.1-1.4	0.4-2.8	2.5-6.2	10.4-10.6	1027.1	-0.01-0.02
HRM2							
Mean	-5.6	-0.5	1.2	6.1	10.3	1027.1	0.03
SD	2.2	2.0	0.8	2.1	0	0	0.02
Range	-10.2- -1	-4.2-3.6	-0.2-3.2	3-10.6	10.2-10.4	1027.1	0.01-0.09